Memorandum 003

Binary Pulsar Emission Variability as a Function of Orbital Phase

Paul Brook & Dustin Madison

2019 April 11

http://nanograv.org/

Abstract

We have looked for changes in the flux density and the pulse profile shape of 24 binary NANOGrav pulsars as they orbit their companions. Only PSR J1713+0747 shows significant pulse profile shape changes and these are only seen in a few isolated isolated profiles. Some pulsars have flux density levels that show trends over their orbital period but they are either of low significance, primarily induced by isolated outlying data points, or both. Incorrectly calibrated flux density measurements also strongly influence some of these trends. Some data sets are very sparse in general or at specific orbital phases. More data will help to confirm or contradict any subtle trends currently observed.

Contents

1 Introduction

A pulsar's radio pulse profile is the average shape of a number of integrated individual pulses. When this number is upwards of $\sim\ 10^5$, a pulsar's profile is typically very stable from epoch to epoch. There are, however, a small but growing number of exceptions in which the pulse profile changes shape; examples occur on various timescales (e.g. Lyne et al., 2010; Kramer et al., 2006; Camilo et al., 2012; Lorimer et al., 2012; Lyne et al., 2017). These changes sometimes seem to be intrinsic to the emission mechanism of the pulsar and it's magnetosphere. Alternatively, pulse profile variations can be caused by geodetic precession (Kramer, 1998; Hotan et al., 2005), torque-free precession (Stairs et al., 2000), propagation through the ionized interstellar medium (IISM), instrumental effects, and radio frequency interference (RFI). In this memorandum, we focus on pulse profile changes that are induced by a radio signal's journey through the IISM. As a pulsar radio signal propagates, there are three main effects that can modify the pulsar shape received at Earth: (1) dispersion, (2) scintillation and (3) scattering.

1. As an electromagnetic signal travels though the IISM, its interaction with free electrons produces a frequency-dependent time delay that scales as ν^{-2}. Dispersion effects on an integrated pulse profile are well understood and correcting for signal dispersion is routine.

2. Inhomogeneities in the IISM induce phase changes in a propagating radio wave. This results in intensity fluctuations acting over a range of bandwidths and timescales. Refractive scintillation causes the flux density of a pulse profile as a whole to vary on long timescales. Diffractive scintillation is the frequency-dependent modulation of pulsar flux density on shorter timescales. If a pulse profile is a composite of a wide range of equally weighted frequency channels, diffractive scintillation can produce pulse profile shape changes.

3. Radio waves traveling through the IISM are scattered and follow different paths to the observer. This can, therefore, lead to the broadening of an observed pulse profile; an intrinsically narrow pulse will broaden due to scattering,

Our line of sight to a pulsar that is in a binary system changes periodically as it moves through its orbit. As the line of sight changes, so too does the environment through which a radio pulse travels to arrive at our telescopes on Earth. Additionally a pulsar's orientation and distance with respect to its companion will change with orbital phase; radiation received by the pulsar magnetosphere from the companion star will vary throughout the orbit. In this memorandum we look for orbital variations in flux density and pulse profile shape as 24 millisecond pulsars (MSPs) move through their binary orbits. In Section 2 we describe the NANOGrav data set used for the analysis, which is discussed in Section 3. In Section 4 we explain the anatomy of the heat maps found in this work. Results are presented in Section 5, which is divided into notable cases of interest (Section 5.1) and all other results (Section 5.2). Conclusions are drawn in Section 6.

2 Data Set

The data analyzed in this paper are a subset of the NANOGrav 11-year data set (Arzoumanian et al., 2018), collected by the Green Bank Telescope (GBT) and the Arecibo Observatory (AO). Pulsars at declinations between 0° and +39° were observed at AO, while all others were observed with the GBT. PSR J1713+0747 was observed with both telescopes. The pulsars and their orbital periods are given in Table 1.

Since 2010, data collected by the GBT have been recorded by the Green Bank Ultimate Pulsar Processing Instrument (GUPPI; DuPlain et al., 2008; Ford et al., 2010). The observations are carried out at center frequencies around 820 and 1500 MHz. Since 2012, data collected at AO have been recorded by the Puerto Rican Ultimate Pulsar Processing Instrument (PUPPI). The observations are carried out at center frequencies around 327 MHz (PSR J2317+1439 only), and 430, 1400, and 2030 MHz. This GUPPI/PUPPI subset was used, as the instruments process a bandwidth of up to 800 MHz. Earlier narrow-bandwidth bandwidth data in the NANOGrav data set were excluded from this analysis due to relatively low signal-to-noise ratio (S/N). GUPPI and PUPPI performed coherent dedispersion and folding in real-time. The data were folded at the dynamically calculated pulsar period using a pre-computed ephemeris to produce the pulse profile, consisting of 2048 phase bins. The pulsar signals were flux and polarization calibrated, and narrow-band RFI was removed in the manner of Gentile et al. (2018). While all the data sets have undergone noise diode calibration as described, full Mueller matrix calibration has also been performed on the 1500 MHz GBT data only. As this method provides more accurate pulse profile information, the GBT 1500 MHz profiles analyzed in this work have had full Mueller matrix calibration applied. Mueller matrix calibration has also recently been applied to AO data by Gentile et al. (2018), but their results have not been included in this analysis.

The dispersion measure (DM) is fitted to the data at almost every observing epoch and applies for a window of up to 14 days, though typically much shorter. In NANOGrav timing analysis, an additional timing delay Δt_{FD} is added to all timing models to compensate for TOA perturbations induced by the frequency-dependence of pulse profile shapes. DM and Δt_{FD} are covariant when finding the best-fit timing model parameters for a pulsar, and so the best-fit DM value is highly dependent on Δt_{FD}. For the purposes of creating the frequency-integrated pulse profiles employed

Table 1: Binary pulsars from the NANOGrav 11-year data set and their orbital periods. Values in parentheses denote the 1σ uncertainty in the preceding digit(s). Table is adapted from Fonseca et al. (2016).

Pulsar	Orbital Period (days)
PSR J0023+0923	0.03484105(11)
PSR J0613−0200	1.0914422(5)
PSR J1012+5307	0.5818176(6)
PSR J1455−3330	32.3622120(3)
PSR J1600−3053	8.8016526(10)
PSR J1614−2230	11.29119744(7)
PSR J1640+2224	55.329717(4)
PSR J1643−1224	25.0725904(3)
PSR J1713+0747	32.34242188(14)
PSR J1738+0333	0.3434297(2)
PSR J1741+1351	11.0033168(4)
PSR J1853+1303	40.76952255(13)
PSR B1855+09	9.2307805(2)
PSR J1903+0327	105.593463(3)
PSR J1909−3744	1.89799095(4)
PSR J1910+1256	21.1291025(2)
PSR J1918−0642	8.3504665(2)
PSR B1953+29	31.4126915(2)
PSR J2017+0603	2.1929208(9)
PSR J2043+1711	1.6239584(2)
PSR J2145−0750	10.16410849(17)
PSR J2214+3000	0.0590817(3)
PSR J2302+4442	51.4299676(5)
PSR J2317+1439	2.313943(4)

in this variability analysis, we have calculated the best-fit DM parameters without the inclusion of Δt_{FD}. Further details of the observations, data reduction, and timing models can be found in Arzoumanian et al. (2018) and references therein.

3 Analysis

Before the profile residuals can be calculated, the observations are processed to ensure that the off-pulse baseline is centered on zero. Any individual observations with highly irregular pulse profiles are treated as the result of RFI or instrumental issues and removed from further analysis. Additionally, the noisiest observations in a data set are considered unreliable and also excluded;

an observation is removed if the standard deviation of the off-pulse region is more than a factor of two larger than the median value taken from the off-pulse regions across all epochs. Only the data sets that consist of 10 or more observations after noisy and unreliable profiles are removed are featured in this work.

We are looking for smooth continuous trends that may occur as a pulsar orbits its companion. These trends may manifest as changes in either the observed flux density or as changes in the shape of the pulse profile. We employ two main analysis techniques: (i) pulse profile alignment and (ii) smoothly modeling how the observations deviate from a constant template profile.

3.1 Pulse Profile Alignment

The NANOGrav collaboration produces pulse profiles for each frequency channel (typically between 5 and 64 over the observing band; Arzoumanian et al. (2015)). The analysis done here, however, looks for changes in pulse profiles that have been frequency-integrated over the observing band. This is done to maximize the S/N to facilitate the principal aim of characterizing the long-term profile behavior in the pulsar. Additionally, when integrating a pulsar signal over a wide observing band, pulse profiles are more susceptible to variations induced by propagation effects (e.g. Pennucci et al., 2014) which is what we are trying to measure. Alignment of these frequency-integrated profiles with the average profile for the data set (the constant profile template) is also essential for the analysis that follows, as the timeseries in each pulse phase bin are modeled independently. This alignment is non-trivial and is carried simultaneously with the flux density normalization. Details of the techniques used are described in Brook et al. (2018).

3.2 Smoothly Modeling how the observations deviate from a constant profile template

Once we have aligned the pulse profiles, we continue our analysis by operating on each of the 2048 individual phase bins in turn. To assess the amount of pulse profile variability for each observed pulse profile, we calculate the differences between each observation and a constant profile template. These differences are termed the *profile residuals.* In order to look for underlying trends in noisy and irregularly sampled data, we use Gaussian process (GP) regression to model the profile residuals in each phase bin. An example of this is shown in the bottom panel of Figure 1. Details of the GP modeling are given in Brook et al. (2018) and references therein. A GP model is produced for each of the 2048 pulse phase bins. The GP length scale has a lower bound of 0.1 of the pulsar's orbit. We find that allowing the GP model to have values less than 0.1 permits the model to deviate sharply when influenced by single data points. This is not suitable for finding the gradual orbital trends in which we are interested. As a result, the GP model may not fit the data well in cases where single outlying data points require a strong deviation of the model over a small section of the orbit. The single bin GP models are subsequently combined to produce *variability maps*, which highlight the differences between an observed pulse profile and a constant profile template as a function of time and pulse phase. Variability map examples are shown in the top two panels of Figure 1 and are explained further in the next section.

4 Explanation of Plots

The heat maps throughout this memorandum show the results of the pulse profile variability anaylsis. Here is an explanation of each of the panels in such variability maps.

Panel A

Variability map depicting how the absolute flux density of the pulse profiles changes with time and pulse phase (with respect to a constant profile template). Red regions indicate where the inferred pulse profile has an excess of flux density compared to the average for the data set. Blue indicates where it has a deficit.The vertical dotted lines in variability maps indicate the orbital phases of the observations that inform the GP models. The unit for all variability maps is the mean of the standard deviation of the off-pulse phase bins for the relevant data set. To the right of each variability map, the average pulse profile for the data set is shown. The map is the combination of 2048 GP models of the profile residuals, one for each phase bin. The solid black line of the grayscale panels of Figure 1 shows an example of a GP modeling the profile residuals of a single phase bin.

Panel B

Map of the standard deviation of the GP models that make up Panel A. An example of this is the gray shaded area of the grayscale panels of Figure 1. Otherwise as Panel A.

Panel C

As Panel A, but the pulse profile have been normalized in order to specifically track changes in the shape of the pulse profiles.

Panel D

As Panel B, but the map is of the standard deviation of the GP models that make up Panel C.

5 Results

We have analyzed 50 data sets. There are no significant changes in pulse profile shape except in PSR J1713+0747 (Panel (C) in Figures 8 and 11). When looking for systematic changes in flux density, the upper panel of Figure 1 provides an example of a variability map that highlights systematic changes in a data set that are not significant when the standard deviation of the GP models is considered. This can be seen by noticing that the values in the second panel down (showing the standard deviation of the GP model) are much larger than those in the top panel (the GP model). Data sets such as this showing systematic but insignificant trends are not considered in the *Notable Cases* section. We instead focus on GP models that show trends with a magnitude at least comparable to the magnitude of their standard deviation.

5.1 Notable Cases

11 data sets show significant flux density changes across the orbit (as reflected by the GP model). Two data sets show significant pulse profile shape changes. These cases are discussed in this section.

5.1.1 PSR J0023+0923 (AO - 430 MHz) - Figures 2 and 3

Panel (A) of Figure 2 shows changes in flux density across the orbital period of the pulsar that are a significant fraction of the standard deviation of the GP models. Figure 3 shows the GP model for a single phase bin which represents the trends seen in the variability map of Panel (A) of Figure 2. It shows that observations for this data set are sparsely sampled at certain orbital phases. A small

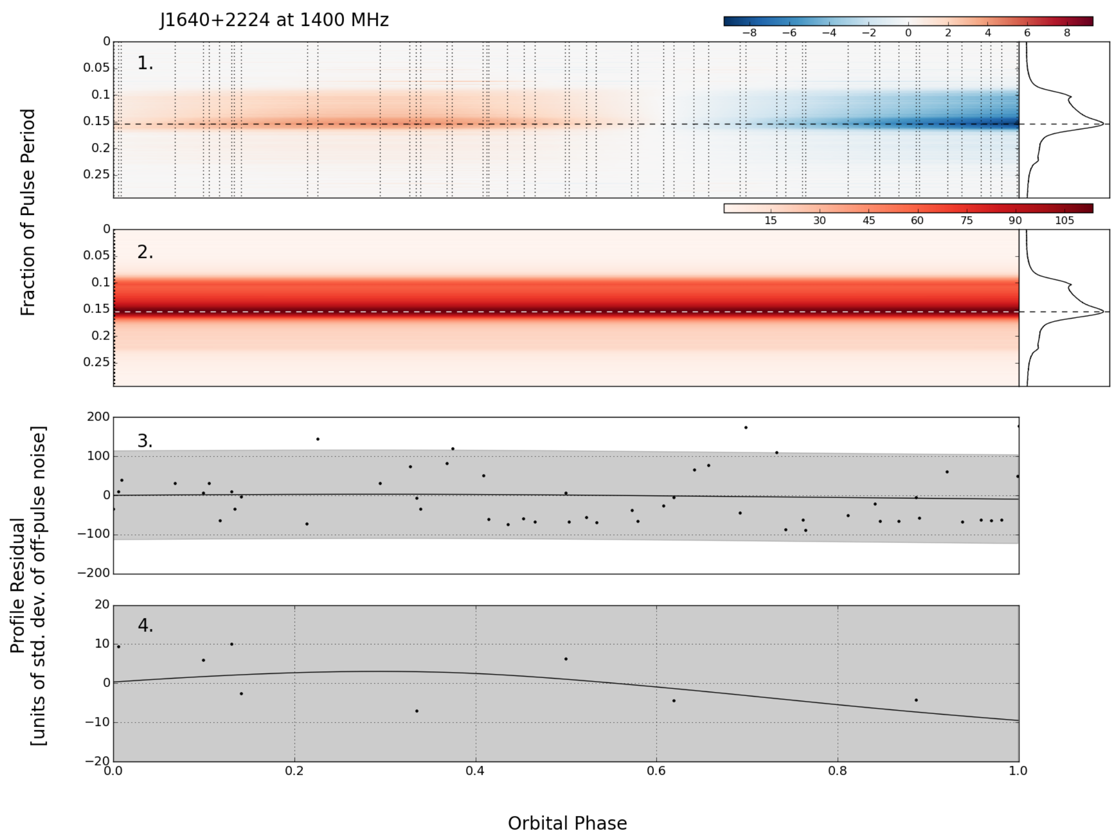

Figure 1: The flux density variability of PSR J1640+2224 at 1400 MHz. Panel 1: Flux density variability map. Red regions indicate where the inferred pulse profile has an excess of flux density compared to the average for the data set. Blue indicates where it has a deficit. Panel 2: Variability map of the standard deviation of the GP model as a function of pulse phase and orbital phase. The vertical dotted lines in variability maps indicate the orbital phases of the observations that inform the GP models. The unit for all variability maps is the mean of the standard deviation of the off-pulse phase bins for the relevant data set. To the right of each variability map, the average pulse profile for the data set is shown. The horizontal dashed line in Panels 1 and 2 shows the pulse phase bin that is depicted in Panels 3 and 4. Panel 3: The GP model for a single phase bin. The solid black line depicts the trend seen in the Panel 1 phase bin depicted by a horizonal dashed line. The gray shaded area of Panel 3 shows the standard deviation of the GP model, as mapped in Panel 2. Panel 4: As Panel 3 but showing only the central region of the y-axis.

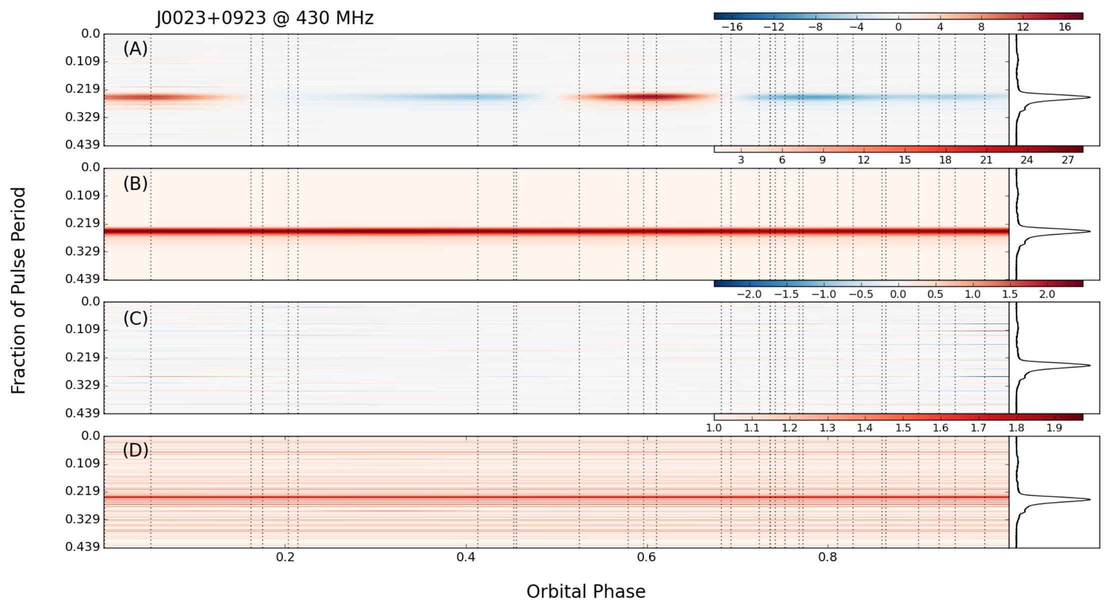

Figure 2: Variability maps for PSR J0023+0923 observed at 430 MHz by AO. As described in Section 4.

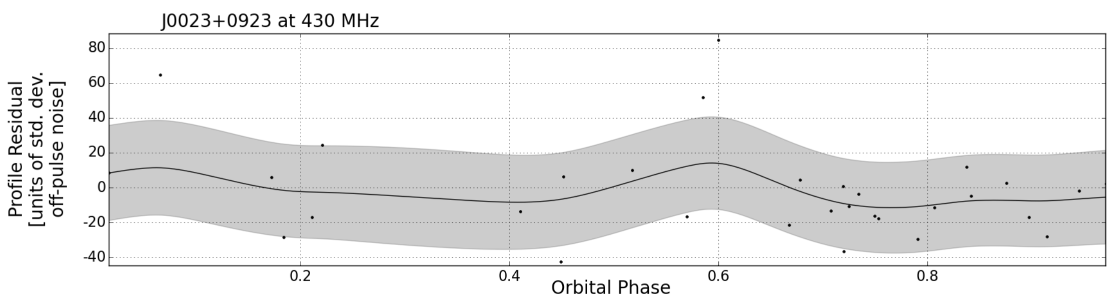

Figure 3: The GP model for a single phase bin which represents the trends seen in the flux density variability map of Panel (A) of Figure 2. The gray shaded area shows the standard deviation of the model.

number of outlying data points affect the GP model, which leads to the systematic trends seen in Figure 2.

5.1.2 PSR J0023+0923 (AO - 1400 MHz) - Figures 4 and 5

Panel (A) of Figure 4 shows significant changes in flux density around orbital phase 0.2. Figure 5 shows the GP model for a single phase bin which represents the trends seen in the variability map of Panel (A) of Figure 4. A single outlying data point in the sparsely sampled data is strongly influencing the GP model.

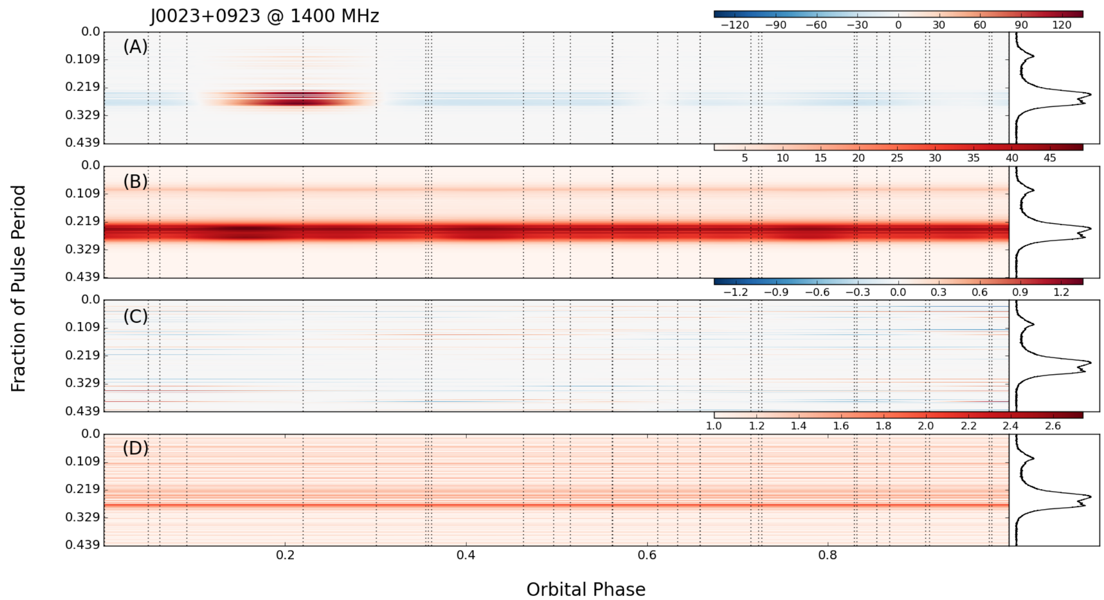

Figure 4: Variability maps for PSR J0023+0923 observed at 1400 MHz by AO. As described in Section 4.

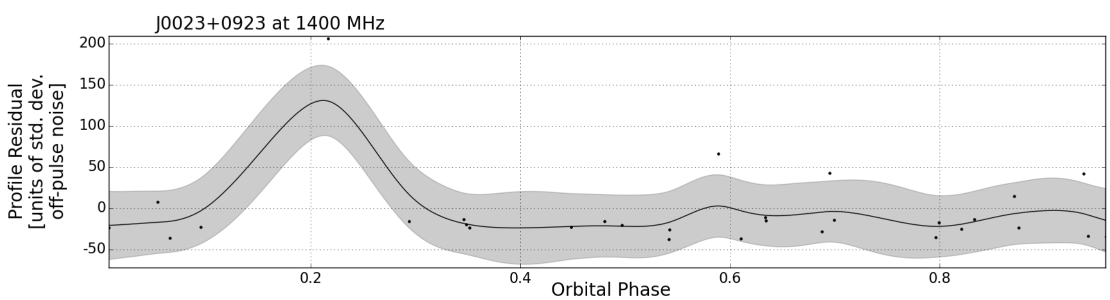

Figure 5: The GP model for a single phase bin which represents the trends seen in the flux density variability map of Panel (A) of Figure 4. The gray shaded area shows the standard deviation of the model.

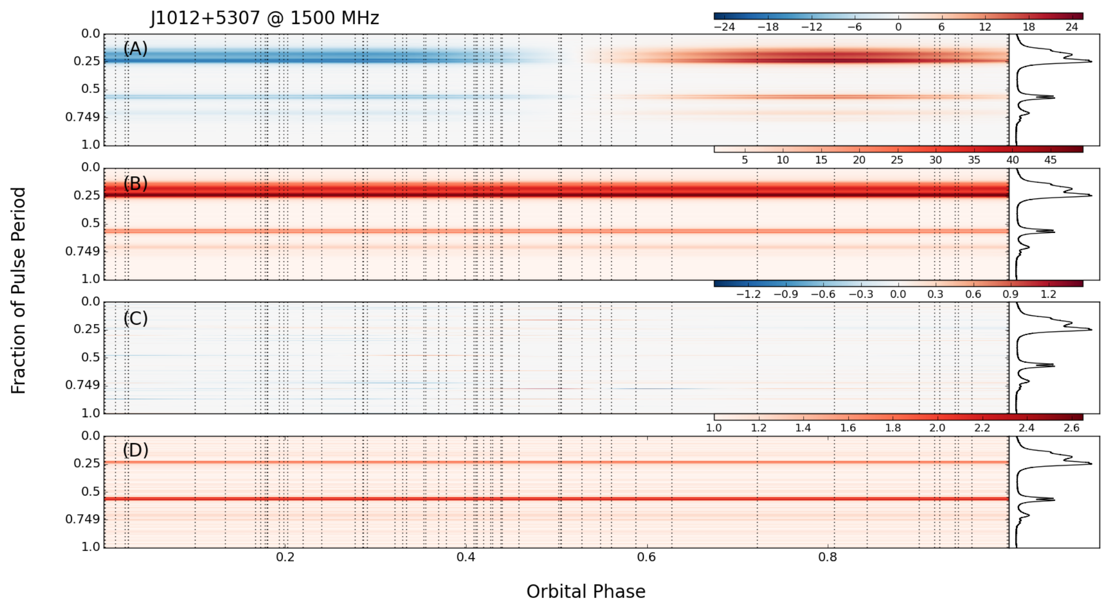

Figure 6: Variability maps for PSR J1012+5307 observed at 1500 MHz by the GBT. As described in Section 4.

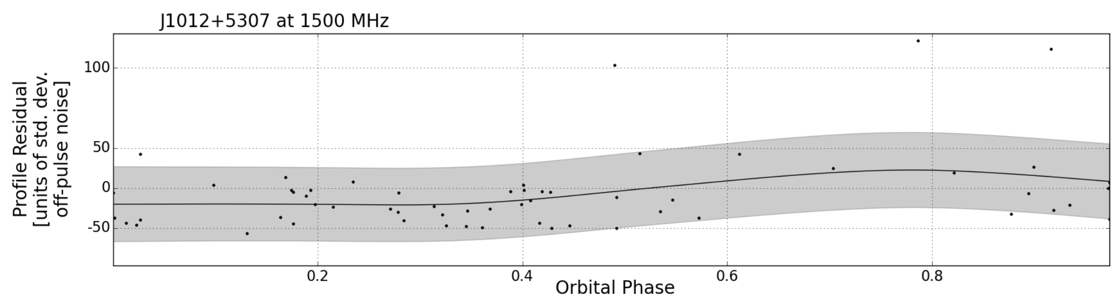

Figure 7: The GP model for a single phase bin which represents the trends seen in the flux density variability map of Panel (A) of Figure 6. The gray shaded area shows the standard deviation of the model.

5.1.3 PSR J1012+5307 (GBT - 1500 MHz) - Figures 6 and 7

Panel (A) of Figure 6 shows changes in flux density across the orbital period of the pulsar that are comparable to the standard deviation of the GP model. Figure 7 shows the GP model for a single phase bin which represents the trends seen in the variability map of Panel (A) of Figure 6. The GP model reflects a slight rise in the average flux density after orbital phases ~ 0.5. There are a also two observations with anomolously high flux density in the latter half, which is also less well sampled than the first half of the data set.

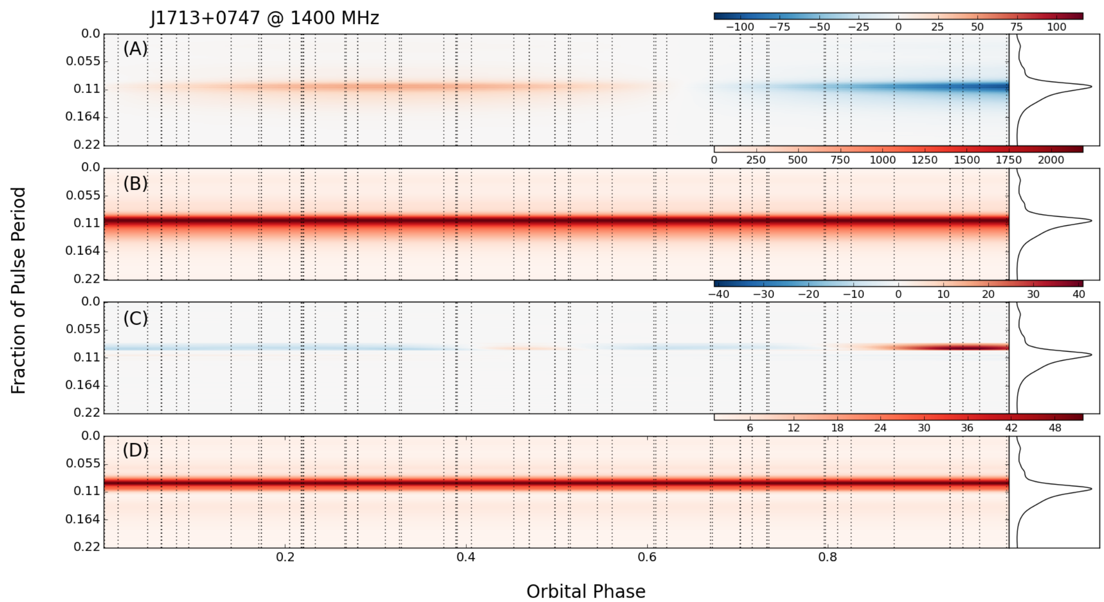

Figure 8: Variability maps for PSR J1713+0747 observed at 1400 MHz by AO. As described in Section 4.

5.1.4 PSR J1713+0747 (AO - 1400 MHz) - Figures 8, 9 and 10

Panel (C) of Figure 8 shows changes in pulse profile shape across the orbital period of the pulsar that are a significant fraction of the standard deviation of the GP model. Figure 9 shows the GP model for a single phase bin which represents the trends seen in the variability map of Panel (C) of Figure 8. It shows that the pulse profile shape changes are primarily influenced by three data points (orbital phases of ~ 0.48, ~ 0.93 and ~ 0.97). These anomalous pulse profiles are shown in Figure 10. These shape changes are discussed in detail in Brook et al. (2018). The cause of the deviant profile shapes is unclear. We do not consider the trend in Panel (A) of Figure 8 as the systematic flux density changes are only a small fraction of the standard deviation of the GP models (as can be seen by comparing the magnitude of values in Panels (A) and (B)).

5.1.5 PSR J1713+0747 (AO - 2030 MHz) - Figures 11, 12, 13 and 14

In this data set, both the flux density and the pulse profile shape show systematic changes. The GP models in panels Panels (A) and (C) of Figure 8 show changes that are a significant fraction of the standard deviation shown in Panels (B) and (D) respectively. The top panel of Figure 12 shows the GP model for a single phase bin which represents the trends seen in the variability map of Panel (A) of Figure 11. It shows that the pulse profile shape changes are primarily influenced

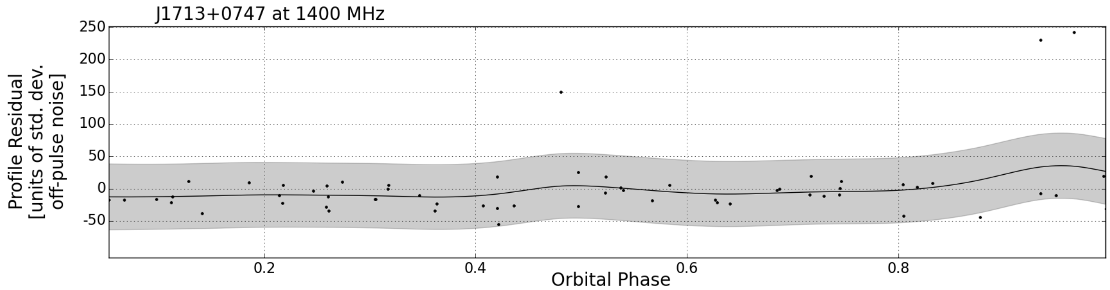

Figure 9: The GP model for a single phase bin which represents the trends seen in the pulse profile shape variability map of Panel (C) of Figure 8. The gray shaded area shows the standard deviation of the model.

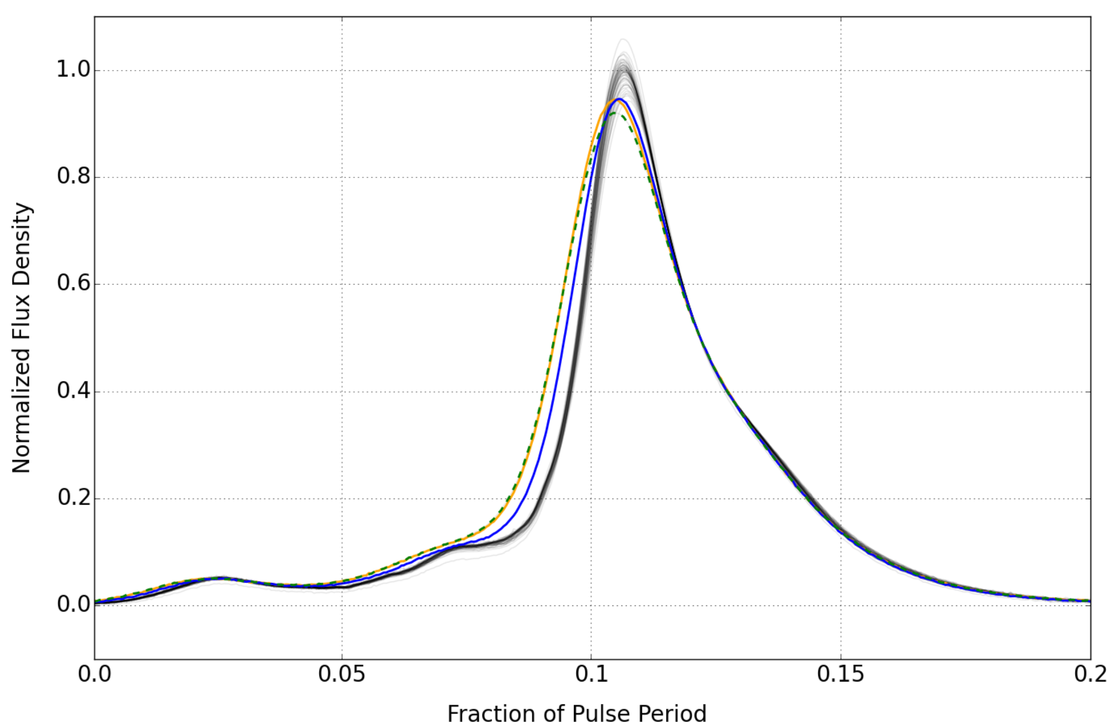

Figure 10: Pulse profile variability seen in PSR J1713+0747, observed by AO at 1400 MHz. The blue, green (dashed) and orange profiles were observed at orbital phases of ~ 0.48, ~ 0.93 and ~ 0.97 respectively. The gray profiles show the other 58 pulse profiles in the data set.

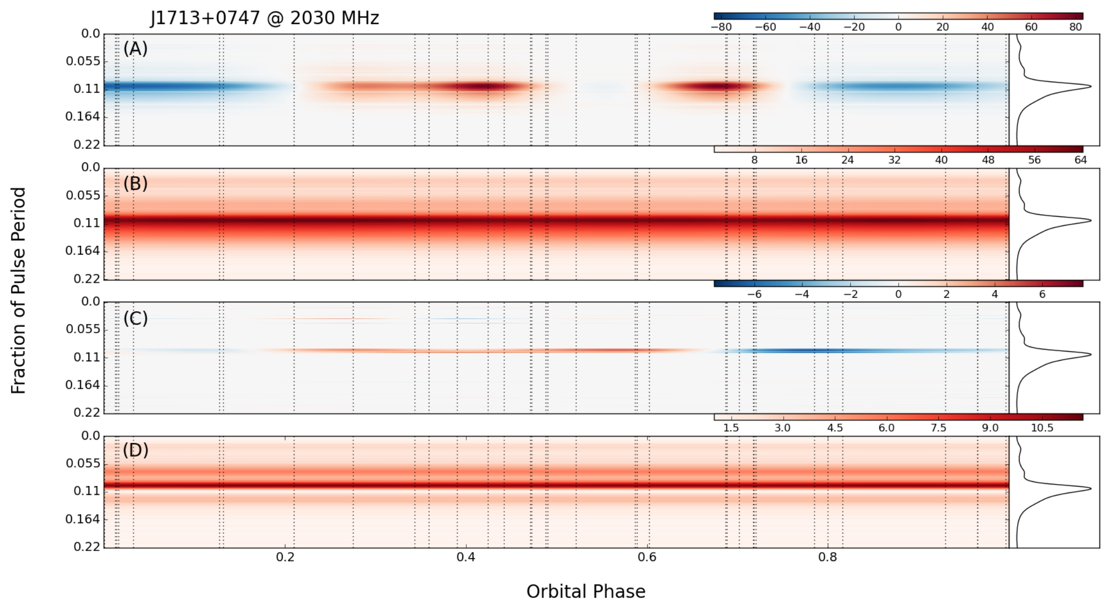

Figure 11: Variability maps for PSR J1713+0747 observed at 2030 MHz by AO. As described in Section 4.

by three data points (at orbital phases of ~ 0.35, ~ 0.48 and ~ 0.71). These brightest three observations have recorded flux density values that are much higher than most other values in the data set. The corresponding pulse profiles are shown in Figure 13. The flux density peak for these profiles are on the order of 10^5 mJy, whereas the level is closer to a few tens or hundreds of mJy for typical observations in the data set. The S/N of these observations is not abnormally high, and suggests that the high flux density is due to miscalibration rather than a very bright signal. The bottom panel of Figure 12 shows the GP model for a single phase bin which represents the trends seen in the variability map of Panel (C) of Figure 11. It shows that the pulse profile shape changes in this data set are primarily influenced by three or four data points. This data set is known to have a number of anomalous pulse profiles shape, which are shown in Figure 14. These shape changes are thought to be caused by RFI and are discussed in detail in Brook et al. (2018).

5.1.6 PSR J1738+0333 (AO - 2030 MHz) - Figures 15, 16 and 17

Panel (A) of Figure 15 shows significant changes in flux density at an orbital phase of ~ 0.2. Figure 16 shows the GP model for a single phase bin which represents the trends seen in the variability map of Panel (A) of Figure 15. The data set is very sparsely sampled and has two

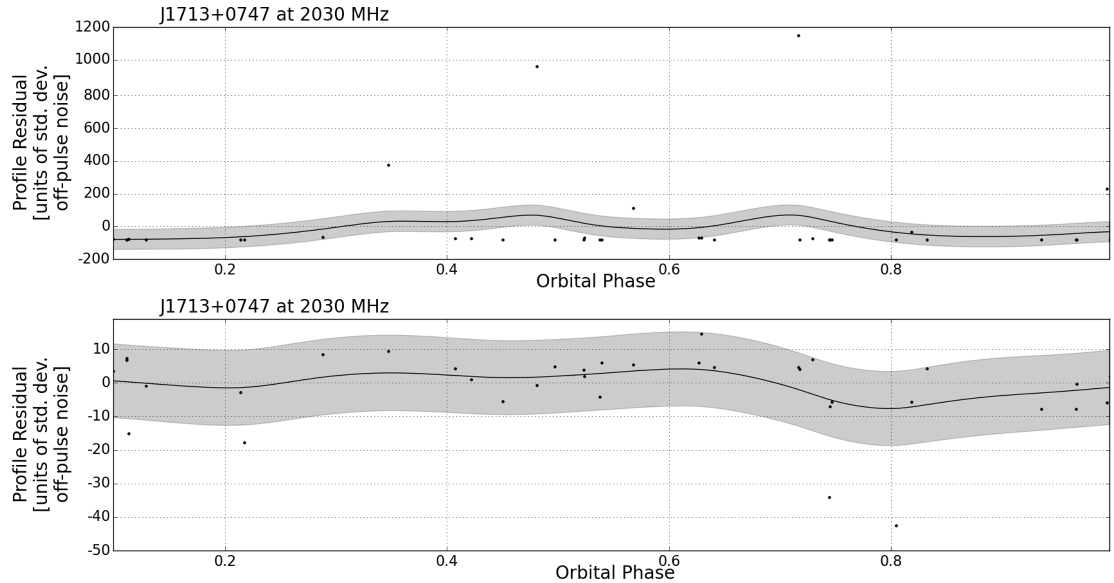

Figure 12: Top panel: The GP model for a single phase bin which represents the trends seen in the flux density variability map of Panel (A) of Figure 11. Bottom panel: The GP model for a single phase bin which represents the trends seen in the pulse profile shape variability map of Panel (C) of Figure 11. In both panels the gray shaded area shows the standard deviation of the model.

outlying points that strongly influence the GP model. These two observations have recorded flux density values that are much higher than other values in the data set, and the corresponding pulse profiles are shown in Figure 17. The flux density peak for these profiles are on the order of 10^6 mJy, whereas it is typically closer to a few mJy. The S/N of these observations suggests that the high flux density is due to miscalibration rather than a very bright signal.

5.1.7 PSR J1903+0327 (AO - 2030 MHz) - Figures 18 and 19

Panel (A) of Figure 18 shows significant changes in flux density across the orbital period of the pulsar. Figure 19 shows the GP model for a single phase bin which represents the trends seen in the variability map of Panel (A) of Figure 18. It shows that observations for this data set are sparsely sampled at certain orbital phases. Two outlying data points affect the GP model, which leads to the systematic trends seen.

5.1.8 PSR J1909−3744 (GBT - 820 MHz) - Figures 20 and 21

Panel (A) of Figure 20 shows changes in flux density across the orbital period of the pulsar that are a significant fraction of the standard deviation of the GP models. Figure 21 shows the GP model for a single phase bin which represents the trends seen in the variability map of Panel (A)

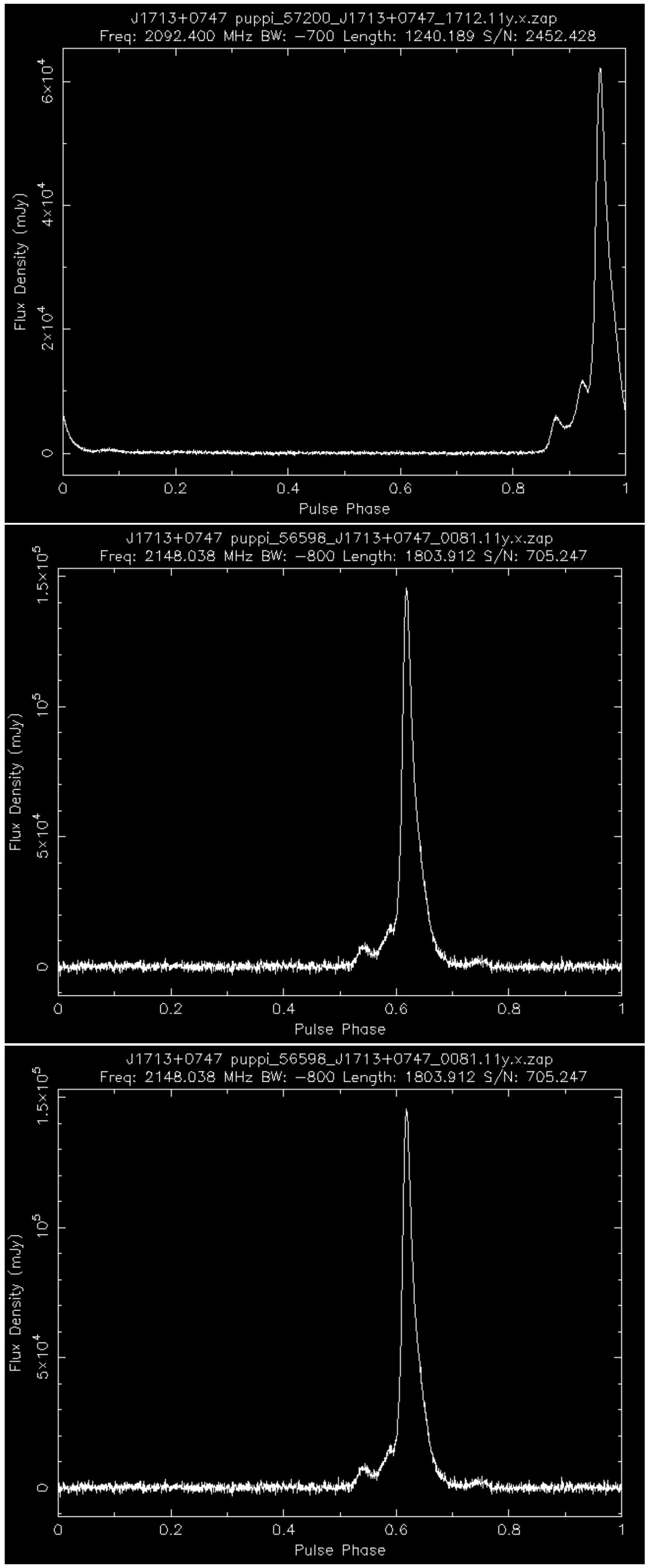

Figure 13: PSR J1713+0747 pulse profiles observed at 2030 MHz by AO that correspond to the three outlying data points in the top panel of Figure 12. All show abnormally high flux density levels, but typical levels of S/N.

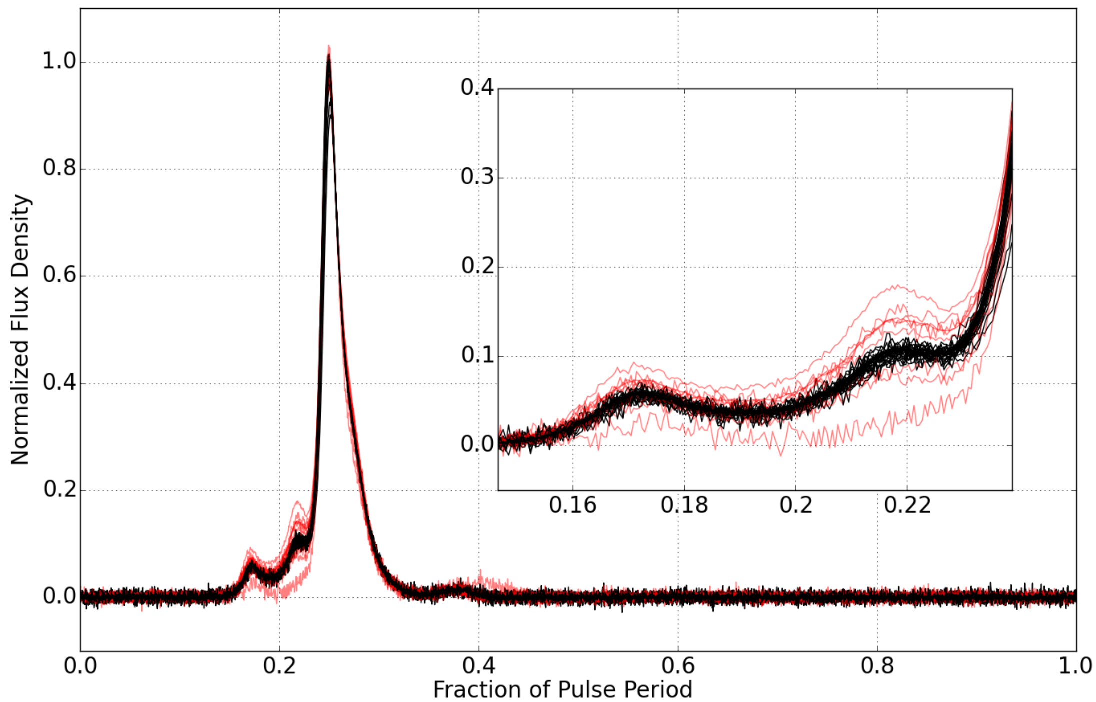

Figure 14: 36 pulse profiles of PSR J1713+0747 observed by AO at 2030 MHz. The red profiles were all observed on or between MJDs 57083 and 57263, which is thought to be a period of prominent RFI. All other profiles are black. Such deviant pulse profile shapes influence the variability seen in Panel (C) of Figure 11 and the bottom panel of Figure 12.

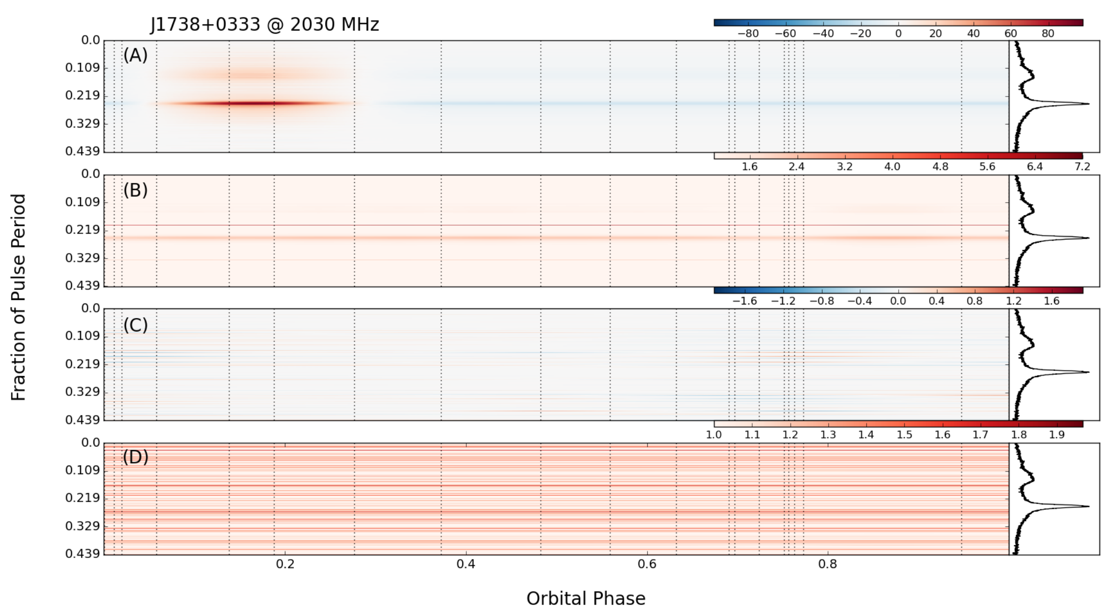

Figure 15: Variability maps for PSR J1738+0333 observed at 2030 MHz by AO. As described in Section 4.

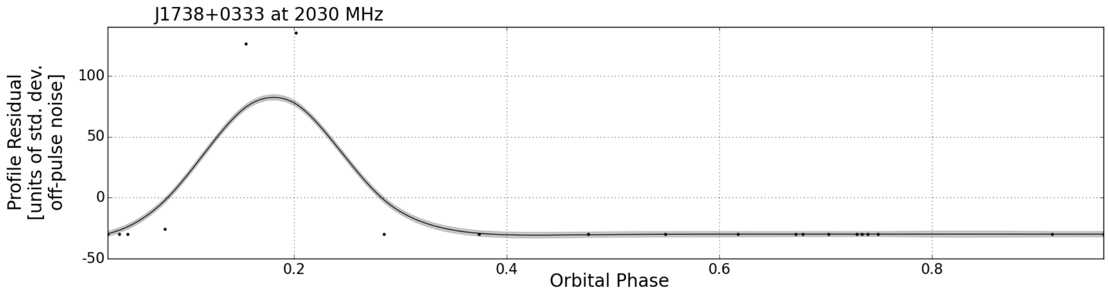

Figure 16: The GP model for a single phase bin which represents the trends seen in the flux density variability map of Panel (A) of Figure 15. The gray shaded area shows the standard deviation of the model.

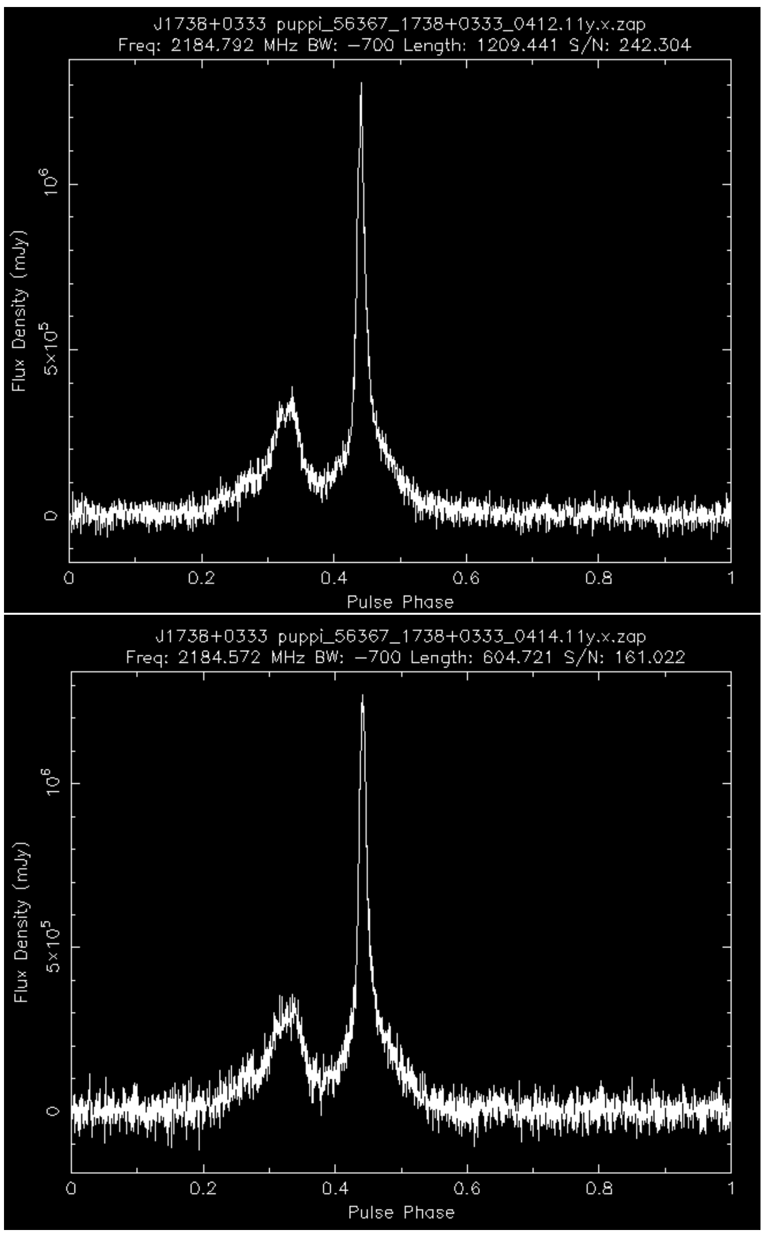

Figure 17: PSR J1738+0333 pulse profiles observed at 2030 MHz by AO that correspond to the two outlying data points in Figure 16. Both show abnormally high flux density levels, but typical levels of S/N.

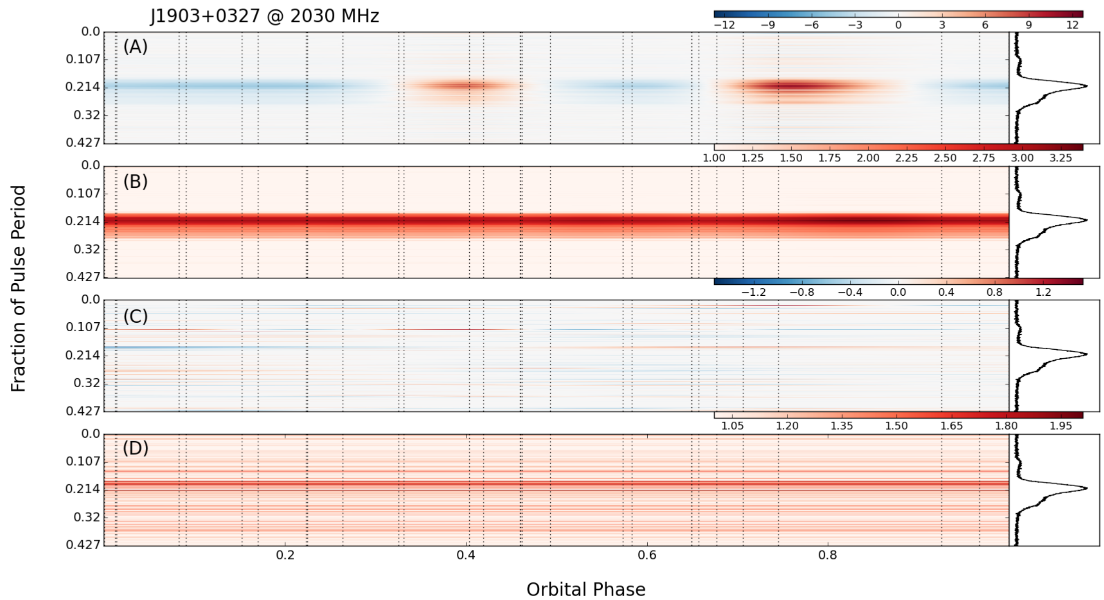

Figure 18: Variability maps for PSR J1903+0327 observed at 2030 MHz by AO. As described in Section 4.

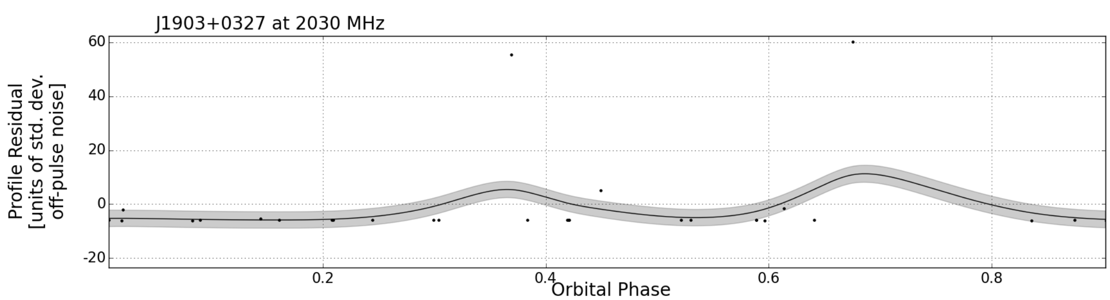

Figure 19: The GP model for a single phase bin which represents the trends seen in the flux density variability map of Panel (A) of Figure 18. The gray shaded area shows the standard deviation of the model.

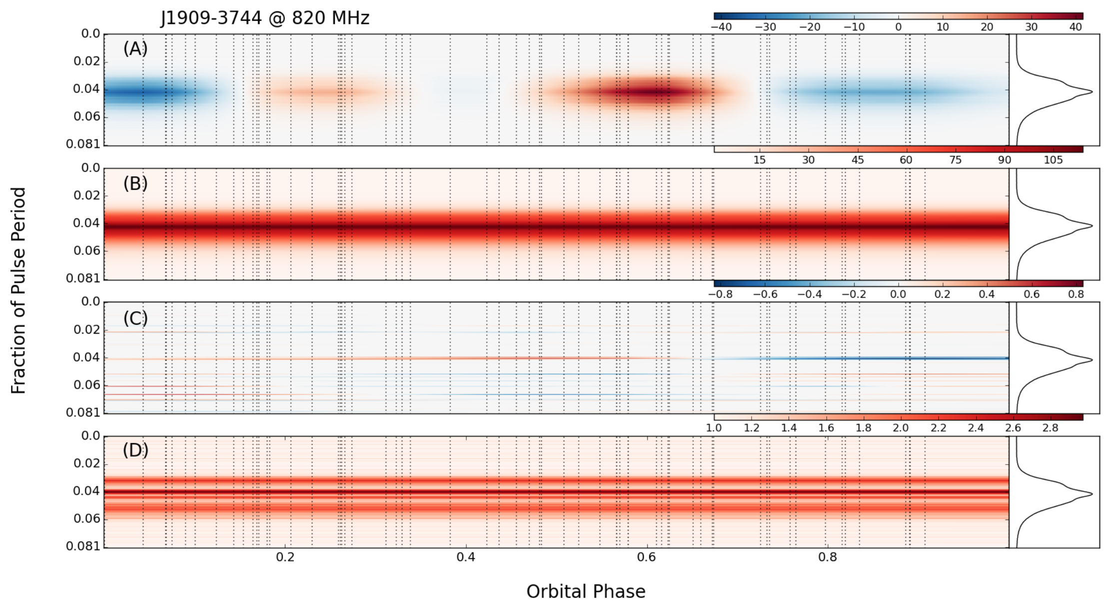

Figure 20: Variability maps for PSR J1909+3744 observed at 820 MHz by the GBT. As described in Section 4.

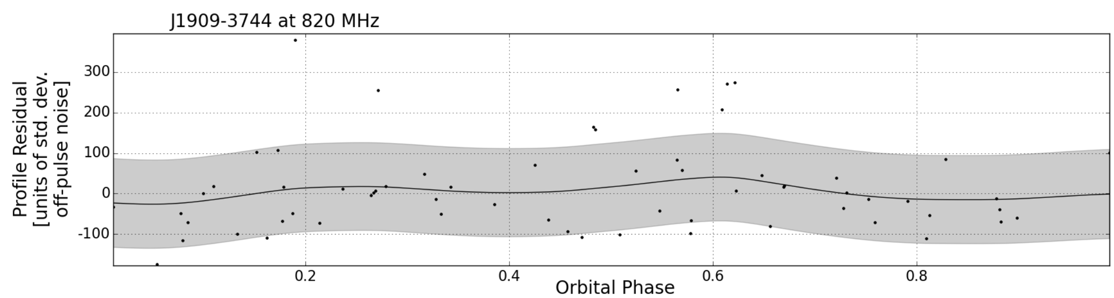

Figure 21: The GP model for a single phase bin which represents the trends seen in the flux density variability map of Panel (A) of Figure 20. The gray shaded area shows the standard deviation of the model.

of Figure 20. A few outlying data points seem to be affecting the GP model, which leads to the subtle systematic trends seen.

5.1.9 PSR J1910+1256 (AO - 2030 MHz) - Figures 22 and 23

Panel (A) of Figure 22 shows changes in flux density that are a significant fraction of the standard deviation of the GP model flux density and occur most strongly around orbital phase ~ 0.25. Figure 23 shows the GP model for a single phase bin which represents the trends seen in the variability map of Panel (A) of Figure 22. A single data point seems to be strongly affecting the GP model, which leads to the systematic trend seen.

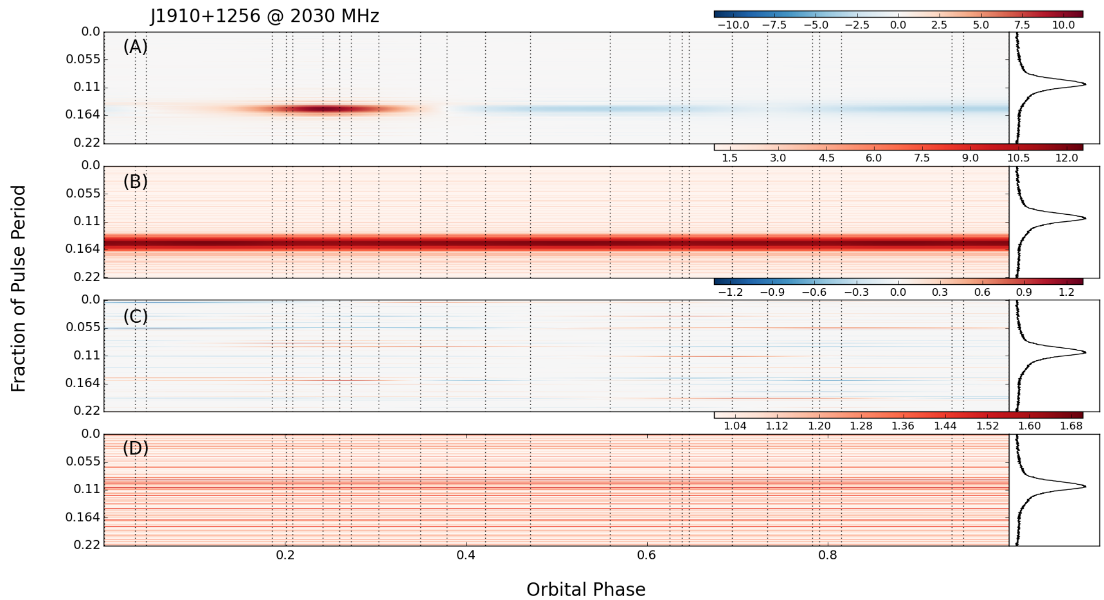

Figure 22: Variability maps for PSR J1910+1256 observed at 2030 MHz by AO. As described in Section 4.

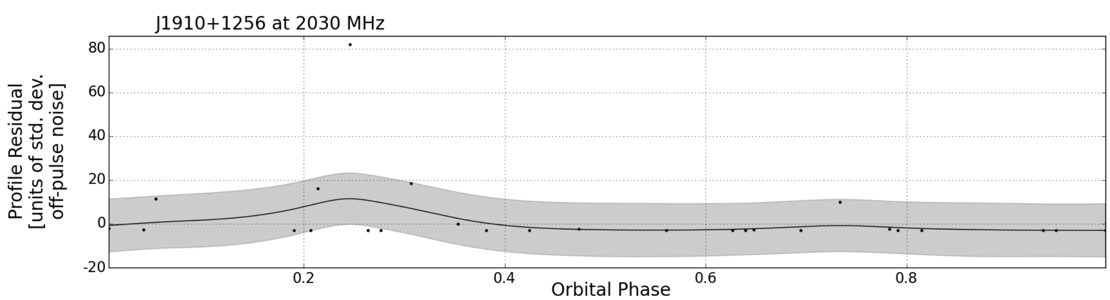

Figure 23: The GP model for a single phase bin which represents the trends seen in the flux density variability map of Panel (A) of Figure 22. The gray shaded area shows the standard deviation of the model.

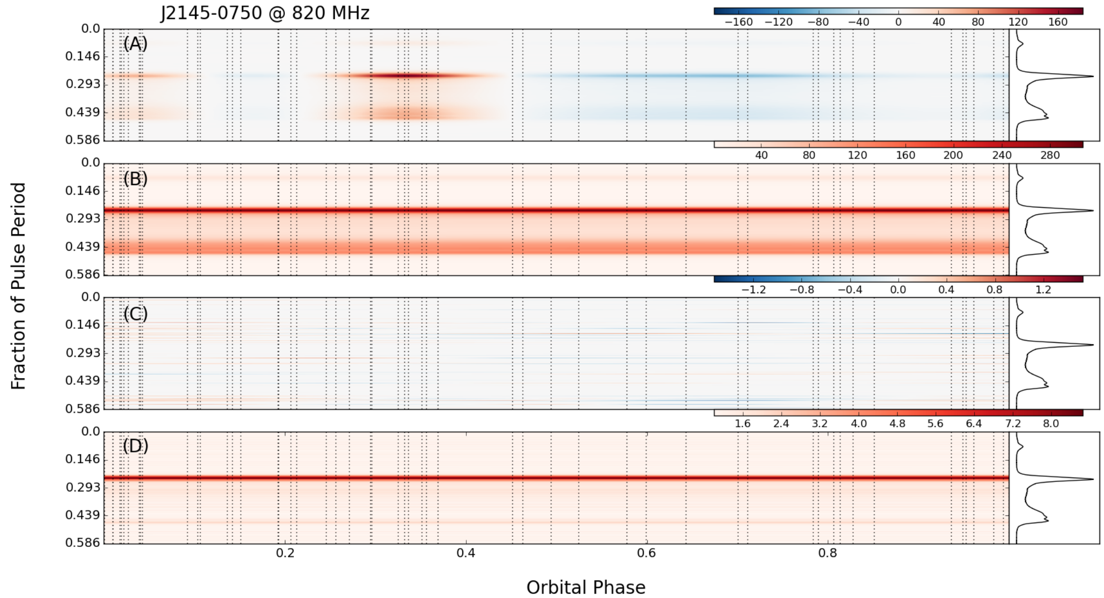

Figure 24: Variability maps for PSR J2145−0750 observed at 820 MHz by the GBT. As described in Section 4.

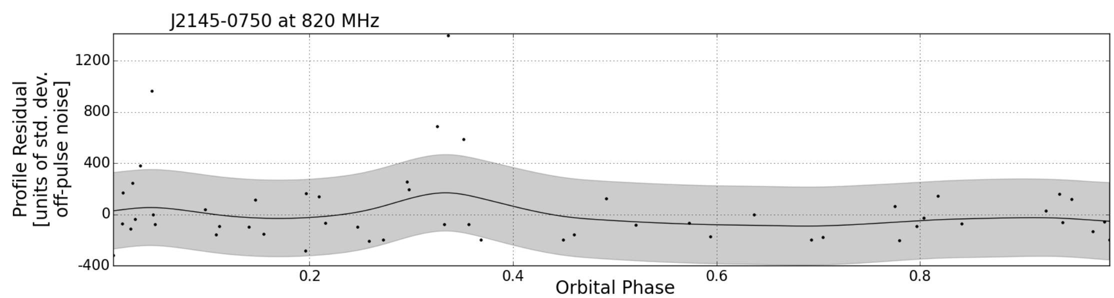

Figure 25: The GP model for a single phase bin which represents the trends seen in the flux density variability map of Panel (A) of Figure 24. The gray shaded area shows the standard deviation of the model.

5.1.10 PSR J2145−0750 (GBT - 820 MHz) - Figures 24 and 25

Panel (A) of Figure 24 shows changes in flux density across the orbital period of the pulsar that are a significant fraction of the standard deviation of the GP models. Figure 25 shows the GP model for a single phase bin which represents the trends seen in the variability map of Panel (A) of Figure 24. A small number of outlying data points, mostly clustered around orbital phases of ~ 0.05 and ~ 0.35, affect the GP model, which leads to the systematic trend seen.

5.1.11 PSR J2214+3000 (AO - 1400 MHz) - Figures 26 and 27

Panel (A) of Figure 26 shows changes in flux density across the orbital period of the pulsar that are a significant fraction of the standard deviation of the GP models. Figure 27 shows the GP

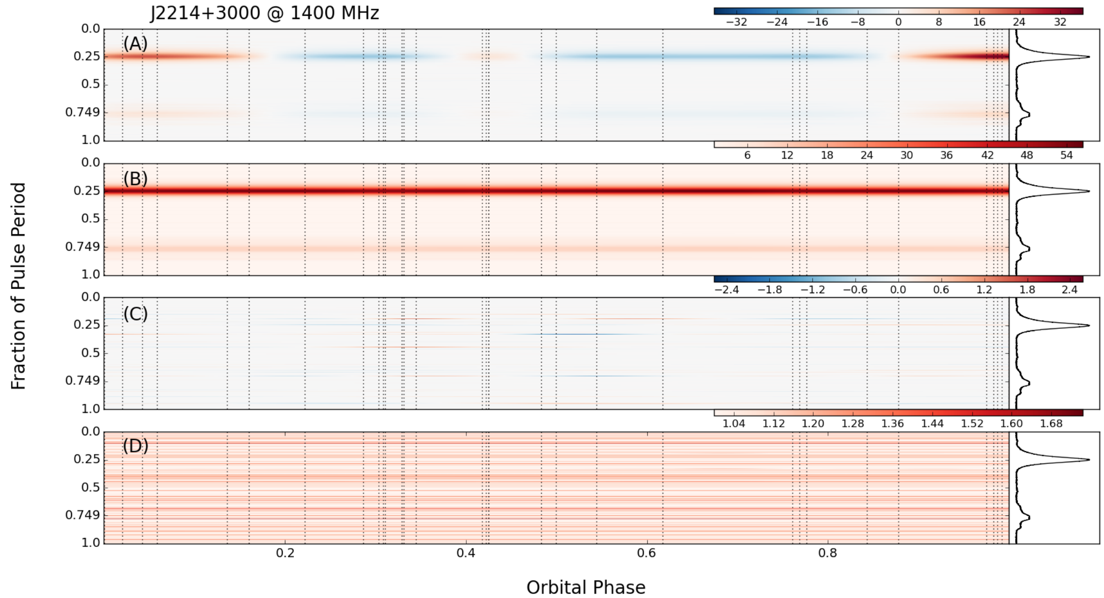

Figure 26: Variability maps for PSR J2214+3000 observed at 1400 MHz by AO. As described in Section 4.

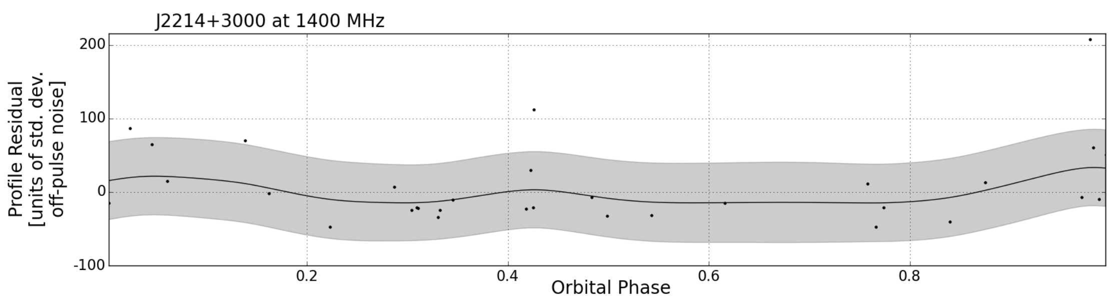

Figure 27: The GP model for a single phase bin which represents the trends seen in the flux density variability map of Panel (A) of Figure 26. The gray shaded area shows the standard deviation of the model.

model for a single phase bin which represents the trends seen in the variability map of Panel (A) of Figure 26. A small number of outlying data points affect the GP model, which leads to the systematic trends seen. The average of the data points between orbital phases 0.8 to 0.2 is greater than the average of the rest of the data.

5.1.12 PSR J2214+3000 (AO - 2030 MHz) - Figures 28, 29 and 30

Panel (A) of Figure 28 shows significant changes in flux density around orbital phase 0.1. Figure 29 shows the GP model for a single phase bin which represents the trends seen in the variability map of Panel (A) of Figure 28. The data set is very sparsely sampled and has one outlying point that strongly influences the GP model. This observation has a recorded flux density value that is much

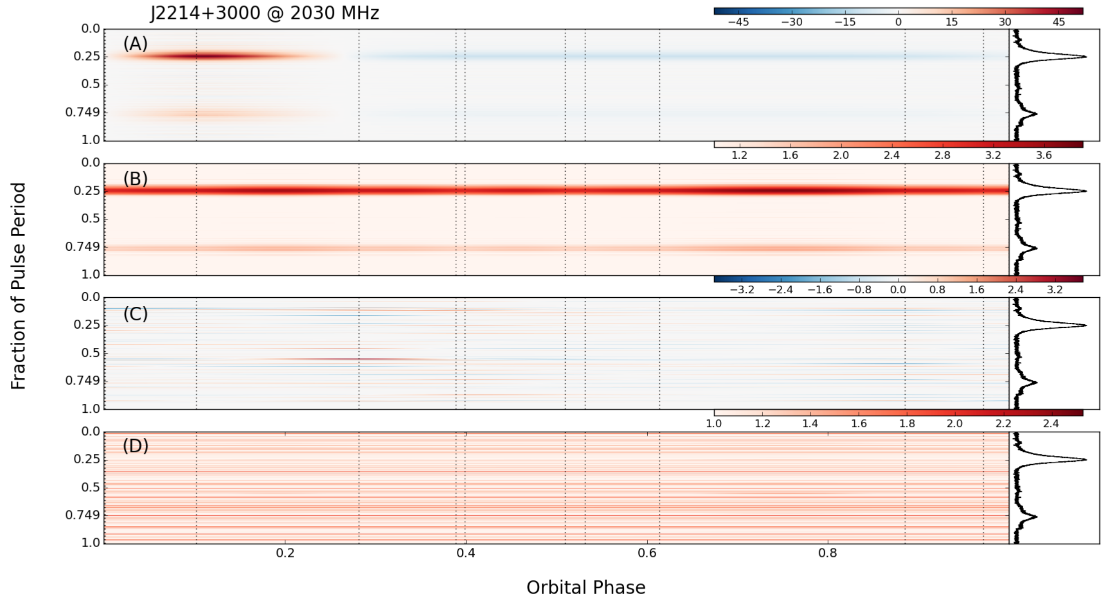

Figure 28: Variability maps for PSR J2214+3000 observed at 2030 MHz by AO. As described in Section 4.

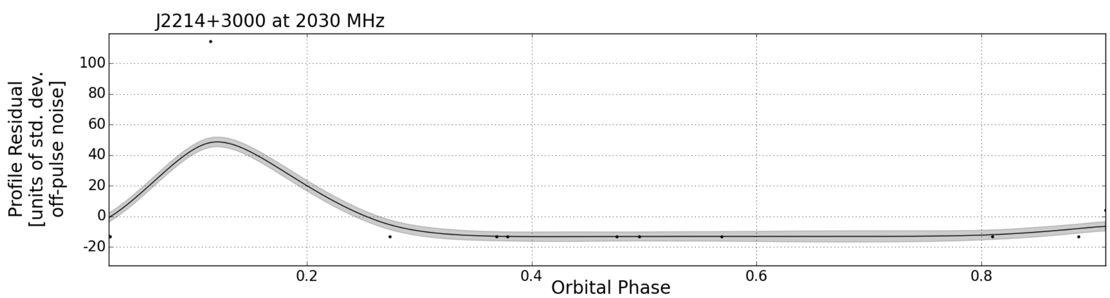

Figure 29: The GP model for a single phase bin which represents the trends seen in the flux density variability map of Panel (A) of Figure 28. The gray shaded area shows the standard deviation of the model.

higher than other values in the data set, and the corresponding pulse profile is shown in Figure 30. The flux density peak for this profile is on the order of 10^5 mJy, whereas it is typically closer to a few mJy. The S/N of the outlying observation suggests that the high flux density is due to miscalibration rather than a very bright signal.

5.2 Other Results - Figures 31 to 68

Variability maps for all 38 data sets not considered notible cases are shown in this section.

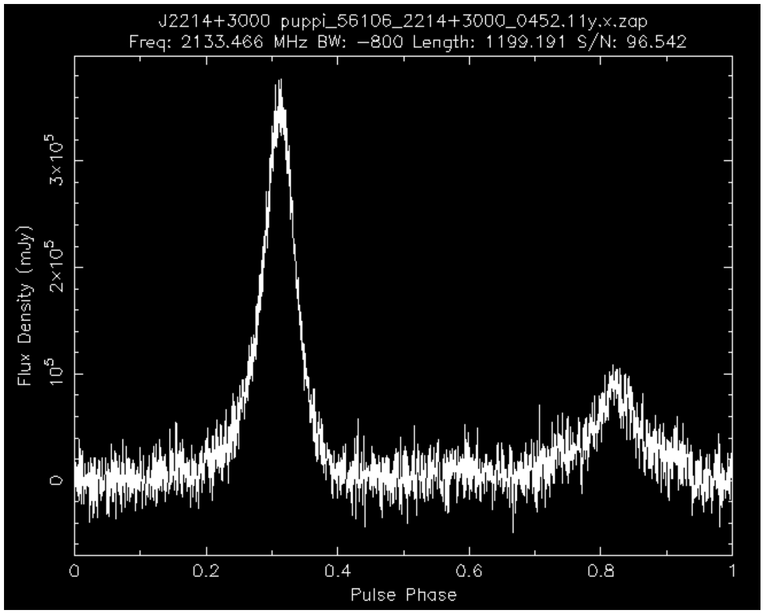

Figure 30: PSR J2214+3000 pulse profiles observed at 2030 MHz by AO that correspond to the outlying data point in Figure 29. The observation shows an abnormally high flux density level, but a typical levels of S/N.

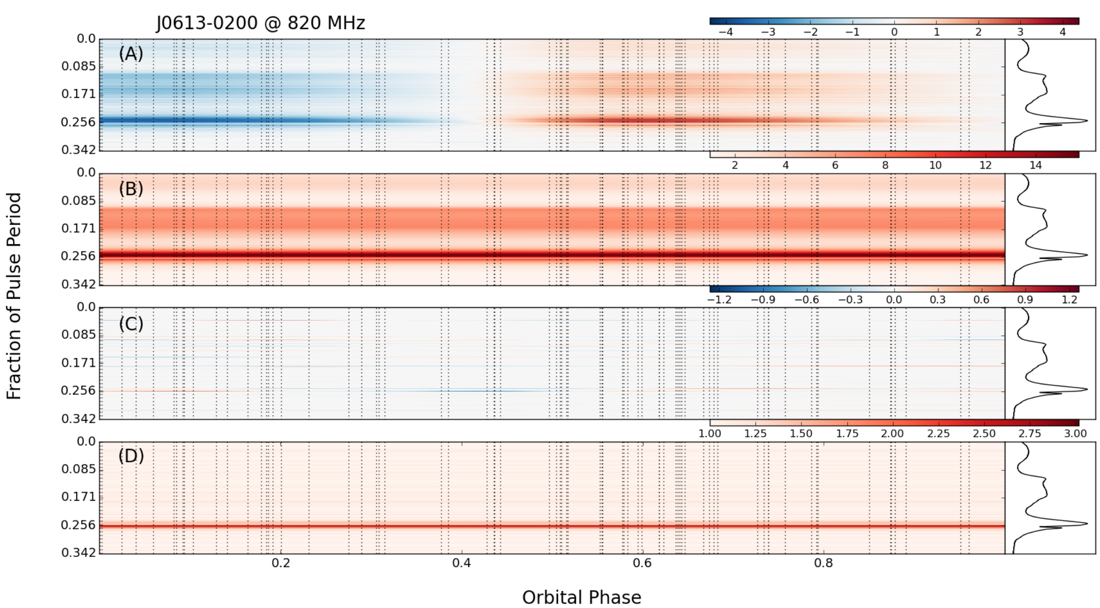

Figure 31: Variability maps for PSR J0613−0200 observed at 820 MHz by the GBT. As described in Section 4.

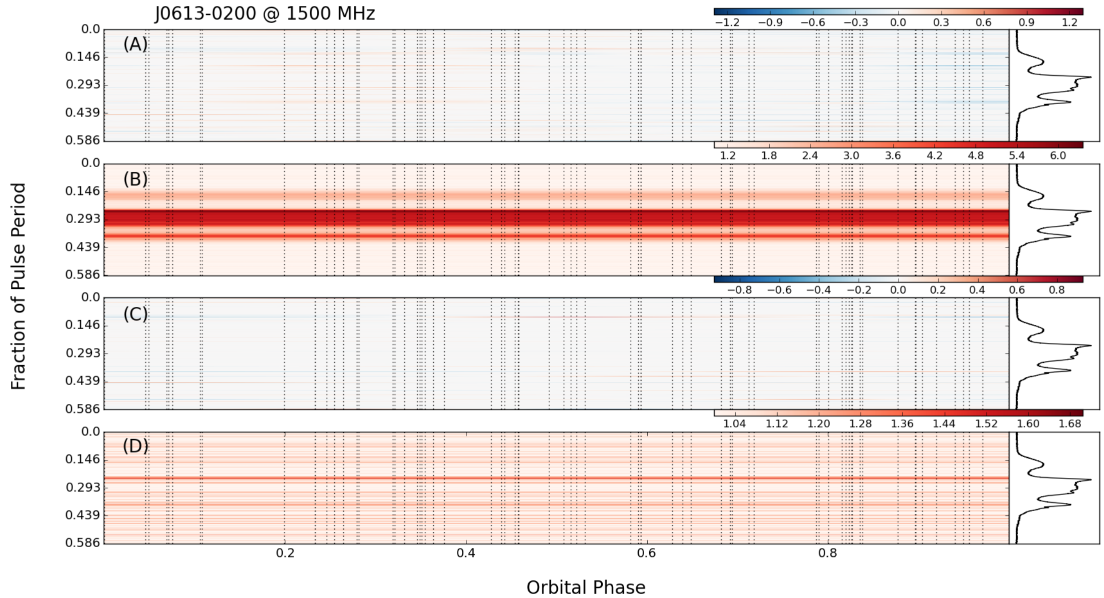

Figure 32: Variability maps for PSR J0613−0200 observed at 1500 MHz by the GBT. As described in Section 4.

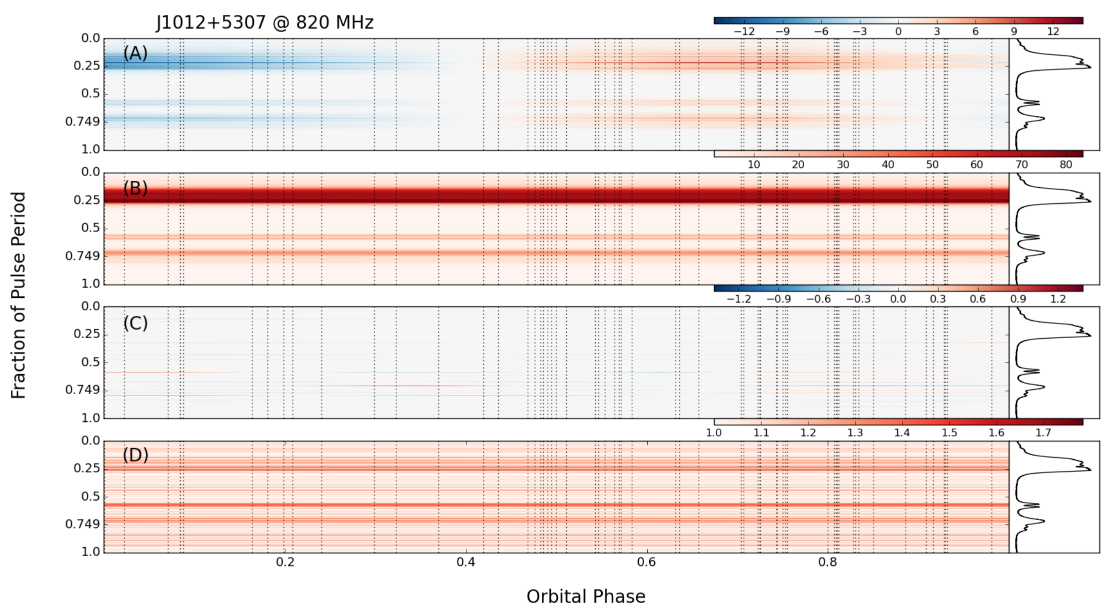

Figure 33: Variability maps for PSR J1012+5307 observed at 820 MHz by the GBT. As described in Section 4.

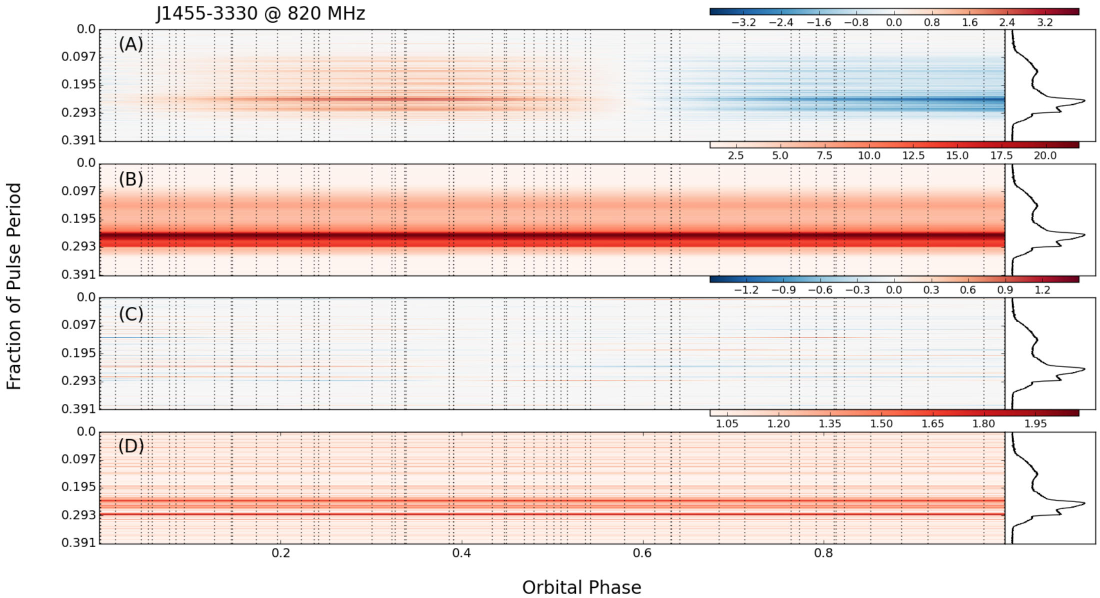

Figure 34: Variability maps for PSR J1455−3330 observed at 820 MHz by the GBT. As described in Section 4.

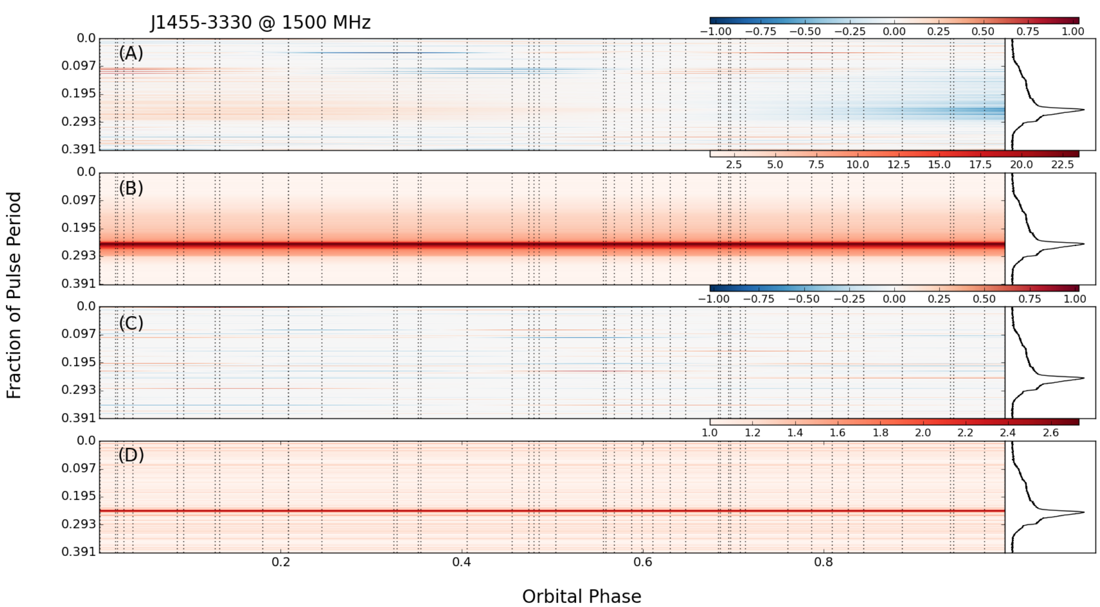

Figure 35: Variability maps for PSR J1455−3330 observed at 1500 MHz by the GBT. As described in Section 4.

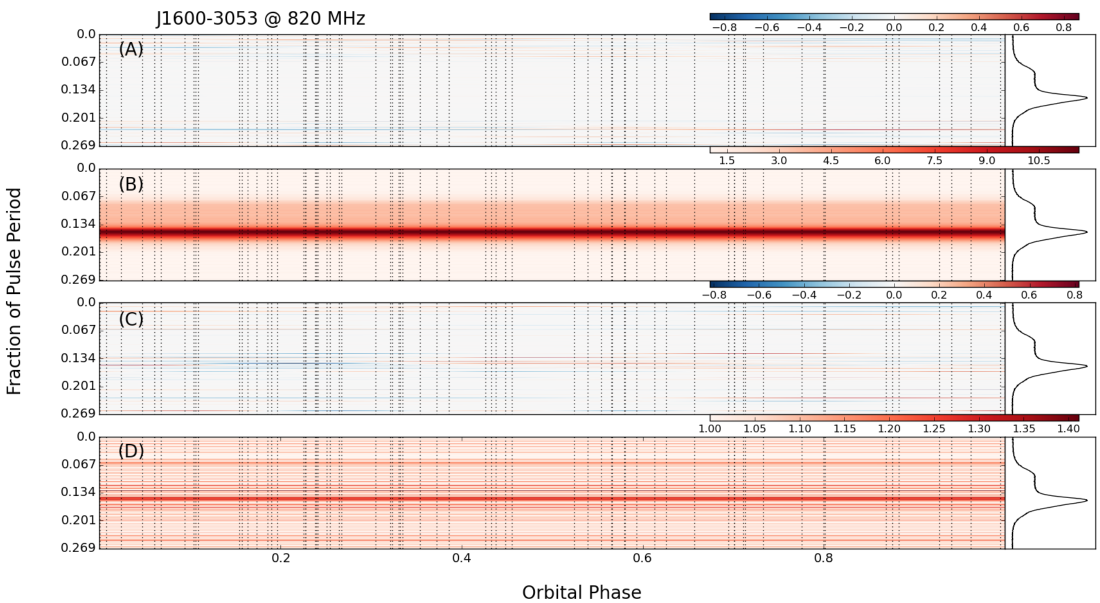

Figure 36: Variability maps for PSR J1600−3053 observed at 820 MHz by the GBT. As described in Section 4.

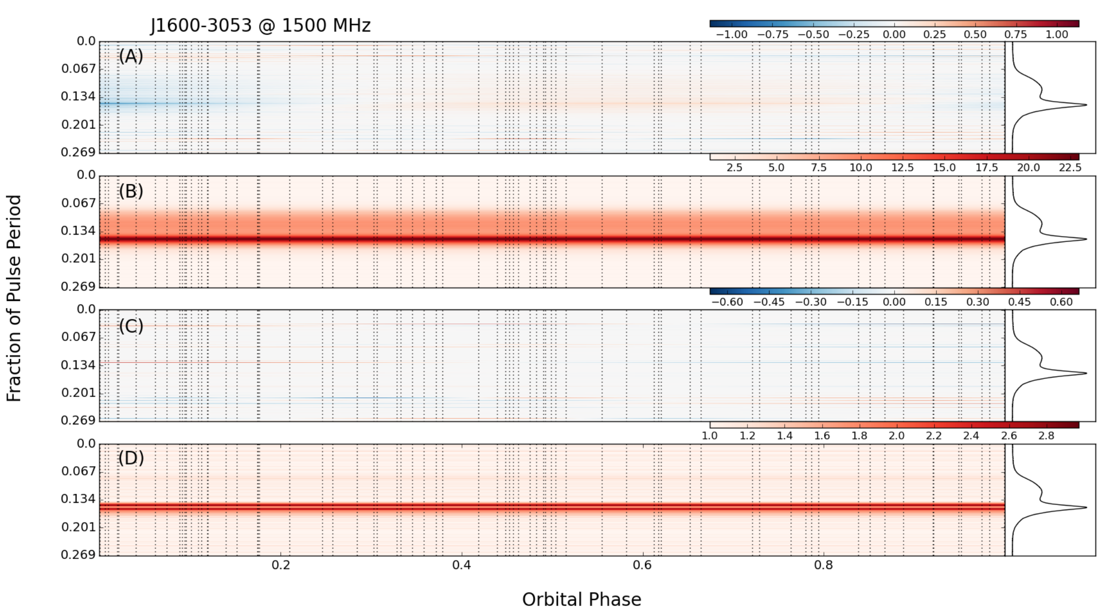

Figure 37: Variability maps for PSR J1600−3053 observed at 1500 MHz by the GBT. As described in Section 4.

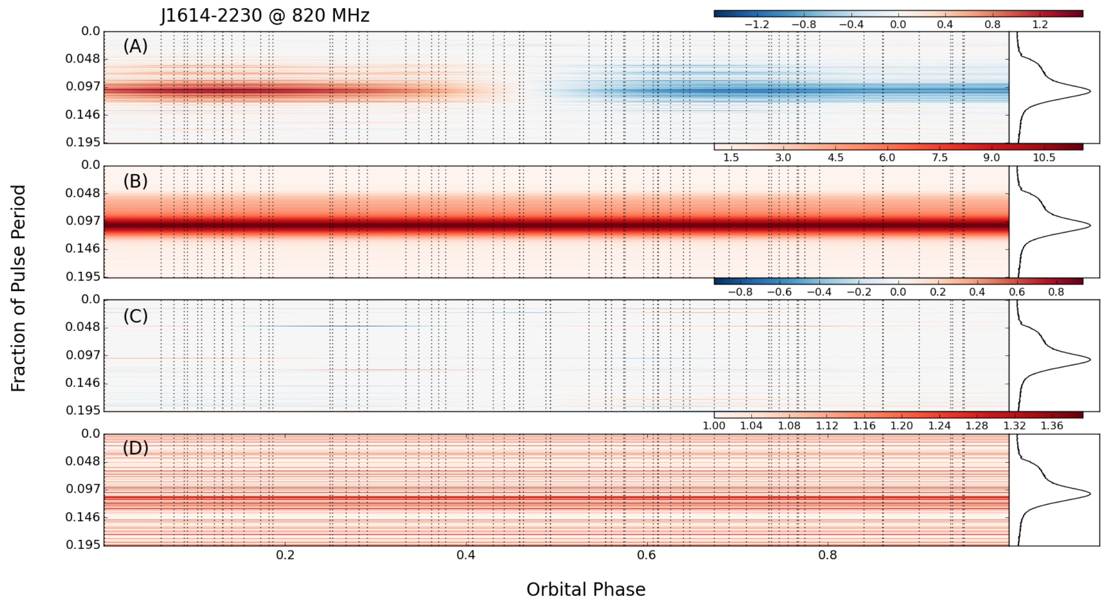

Figure 38: Variability maps for PSR J1614−2230 observed at 820 MHz by the GBT. As described in Section 4.

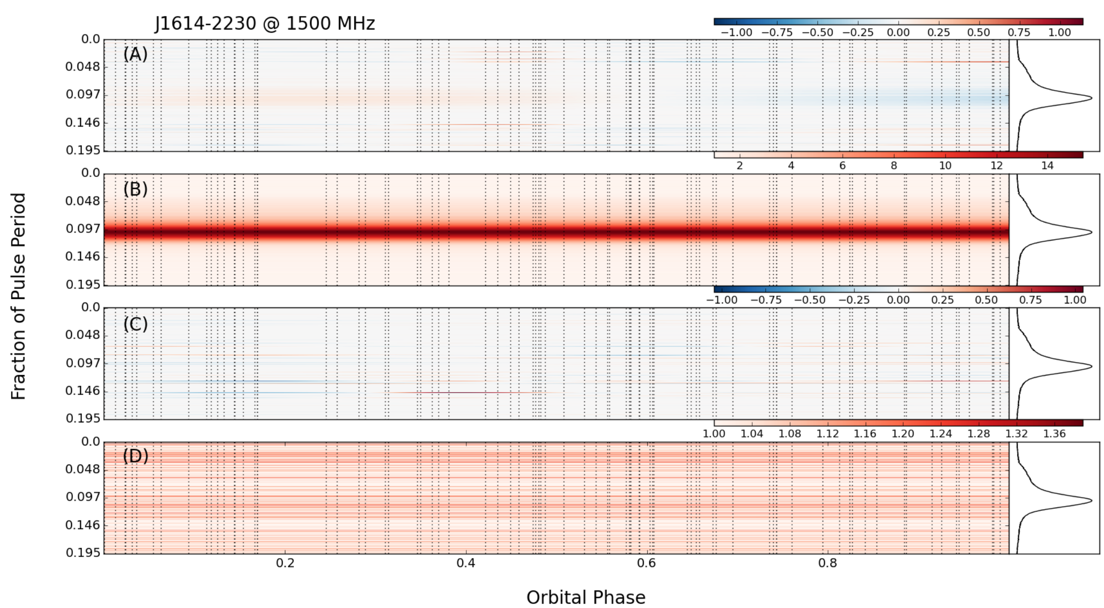

Figure 39: Variability maps for PSR J1614−2230 observed at 1500 MHz by GBT. As described in Section 4.

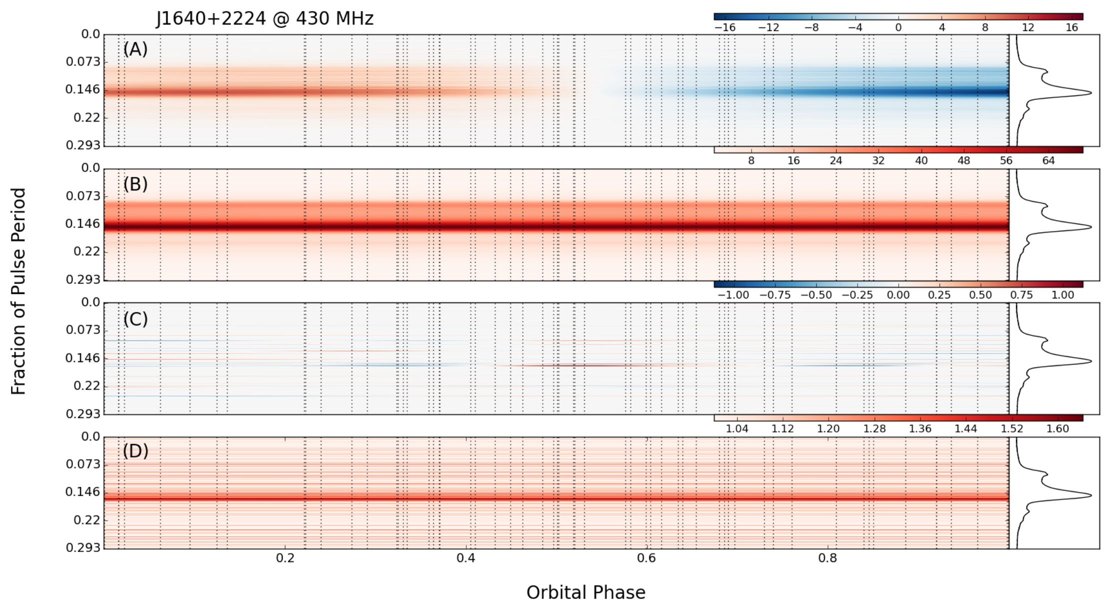

Figure 40: Variability maps for PSR J1640+2224 observed at 430 MHz by AO. As described in Section 4.

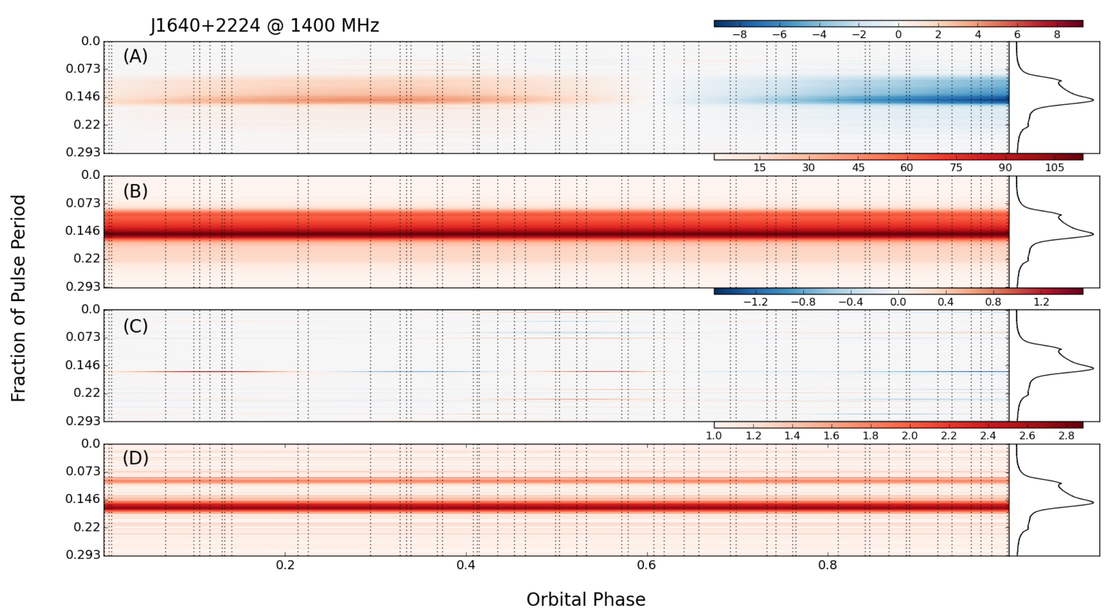

Figure 41: Variability maps for PSR J1640+2224 observed at 1400 MHz by AO. As described in Section 4.

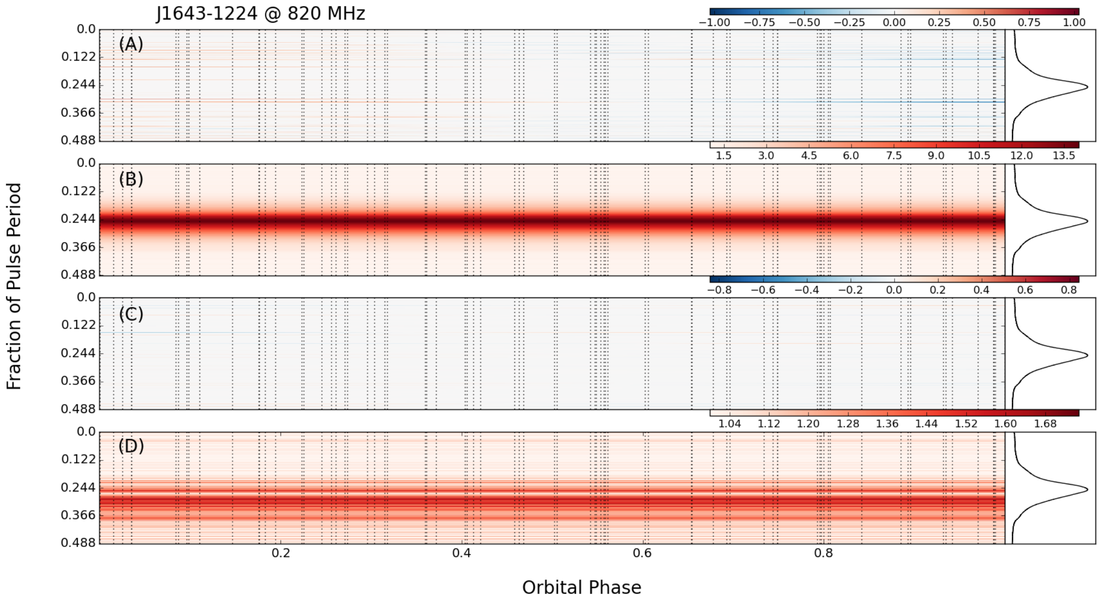

Figure 42: Variability maps for PSR J1643−1224 observed at 820 MHz by the GBT. As described in Section 4.

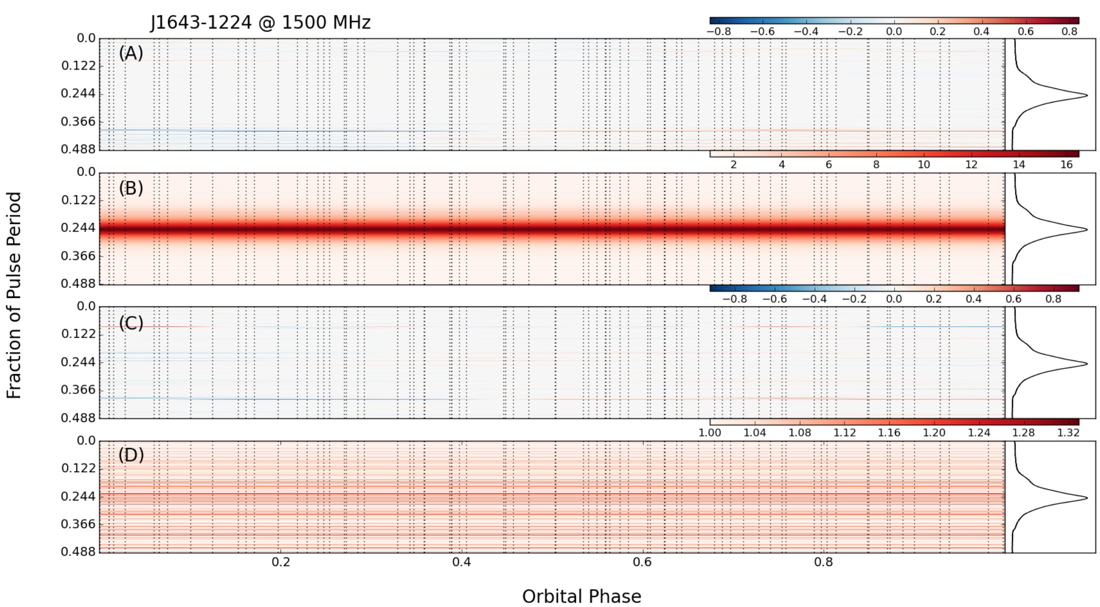

Figure 43: Variability maps for PSR J1643−1224 observed at 1500 MHz by the GBT. As described in Section 4.

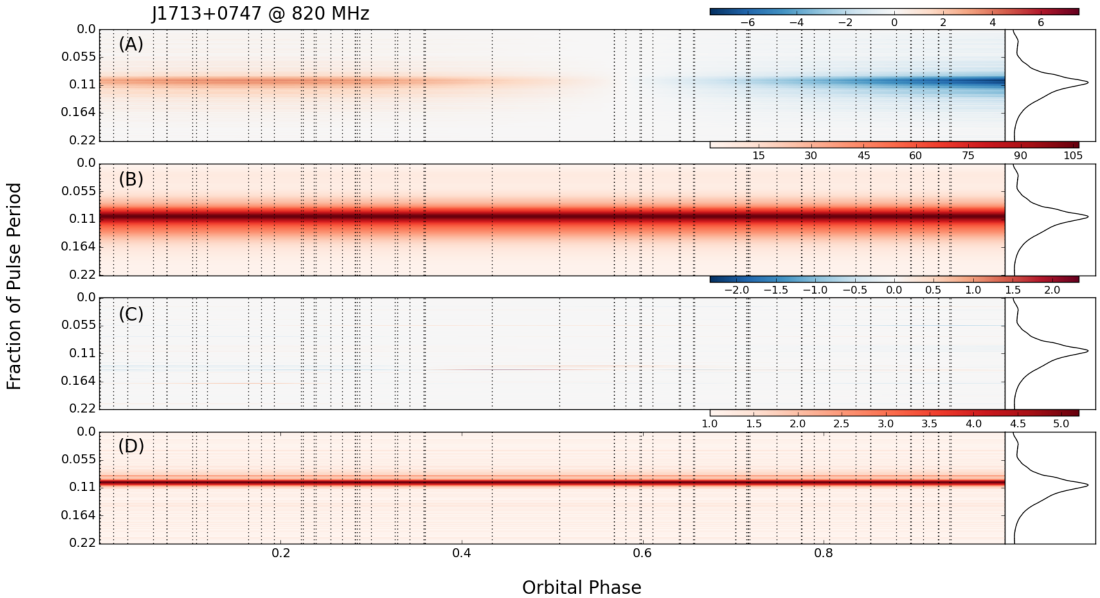

Figure 44: Variability maps for PSR J1713+0747 observed at 820 MHz by the GBT. As described in Section 4.

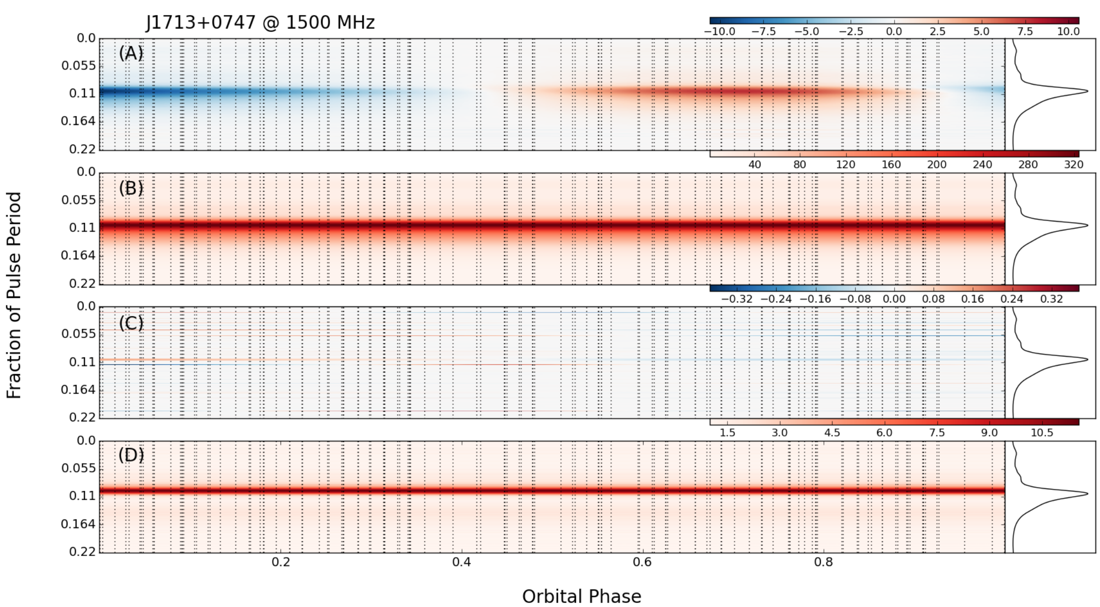

Figure 45: Variability maps for PSR J1713+0747 observed at 1500 MHz by the GBT. As described in Section 4.

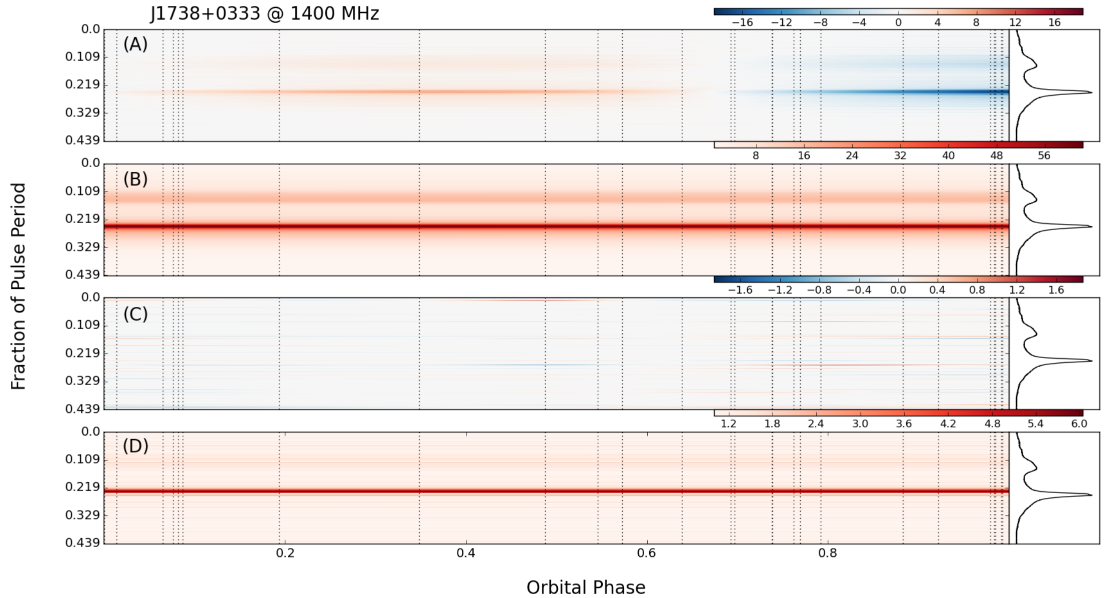

Figure 46: Variability maps for PSR J1738+0333 observed at 1400 MHz by AO. As described in Section 4.

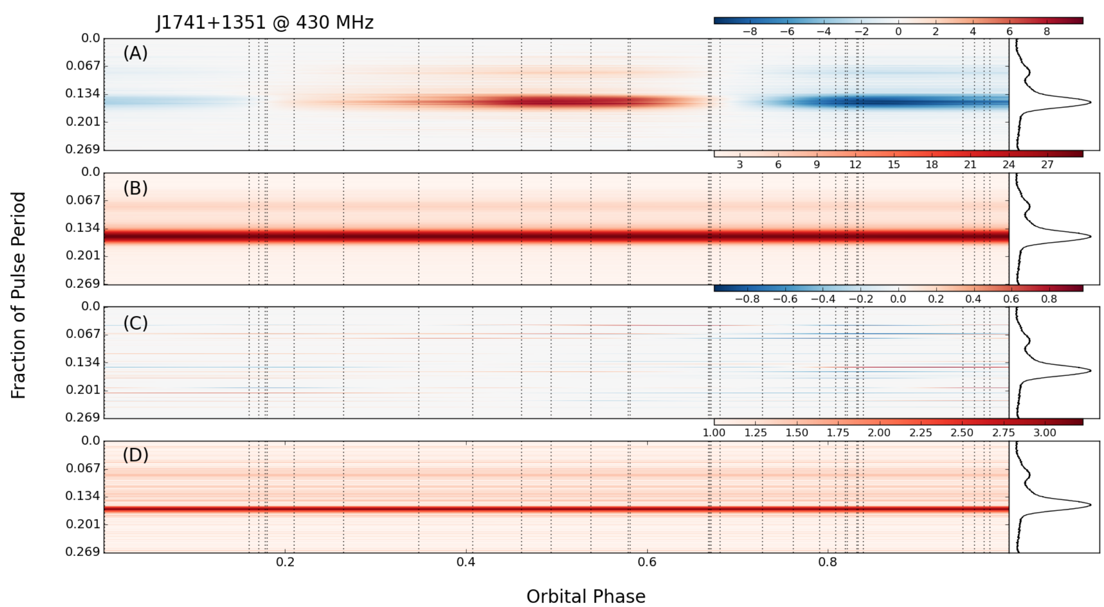

Figure 47: Variability maps for PSR J1741+1351 observed at 430 MHz by AO. As described in Section 4.

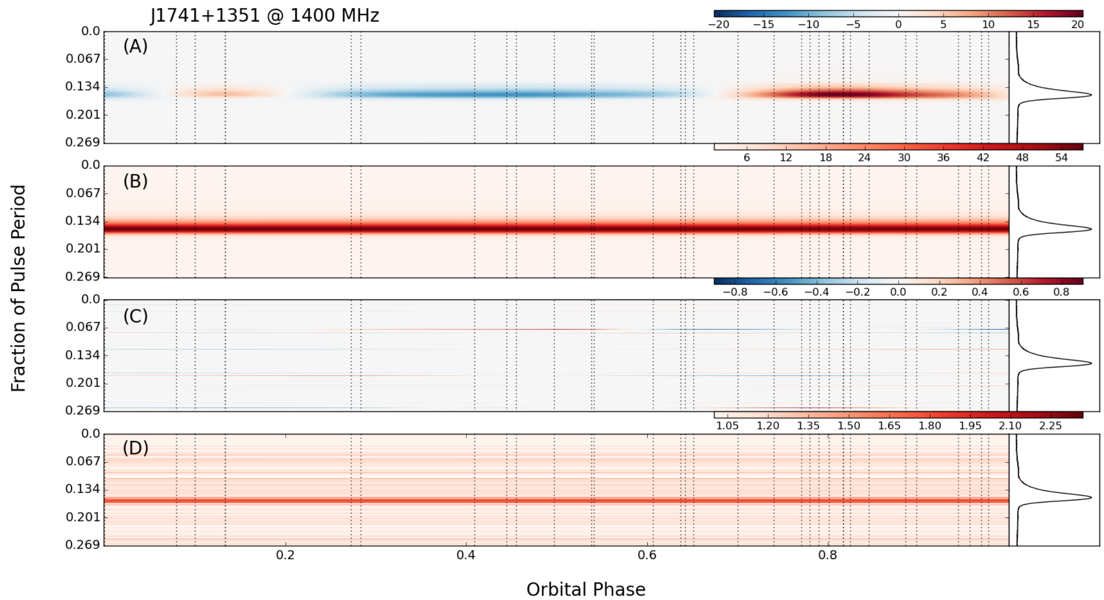

Figure 48: Variability maps for PSR J1741+1351 observed at 1400 MHz by AO. As described in Section 4.

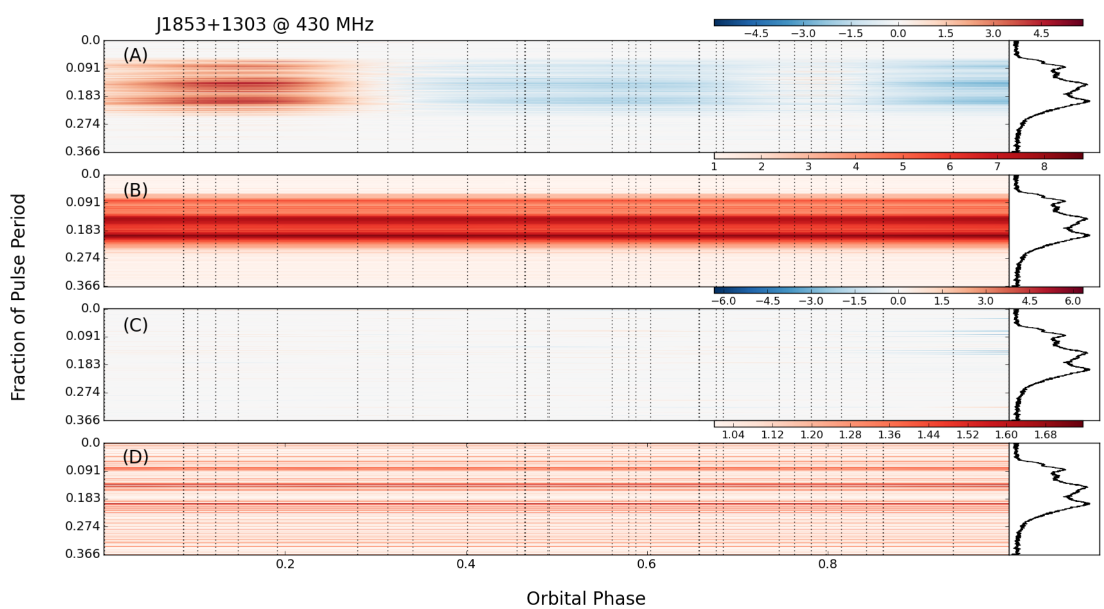

Figure 49: Variability maps for PSR J1853+1303 observed at 430 MHz by AO. As described in Section 4.

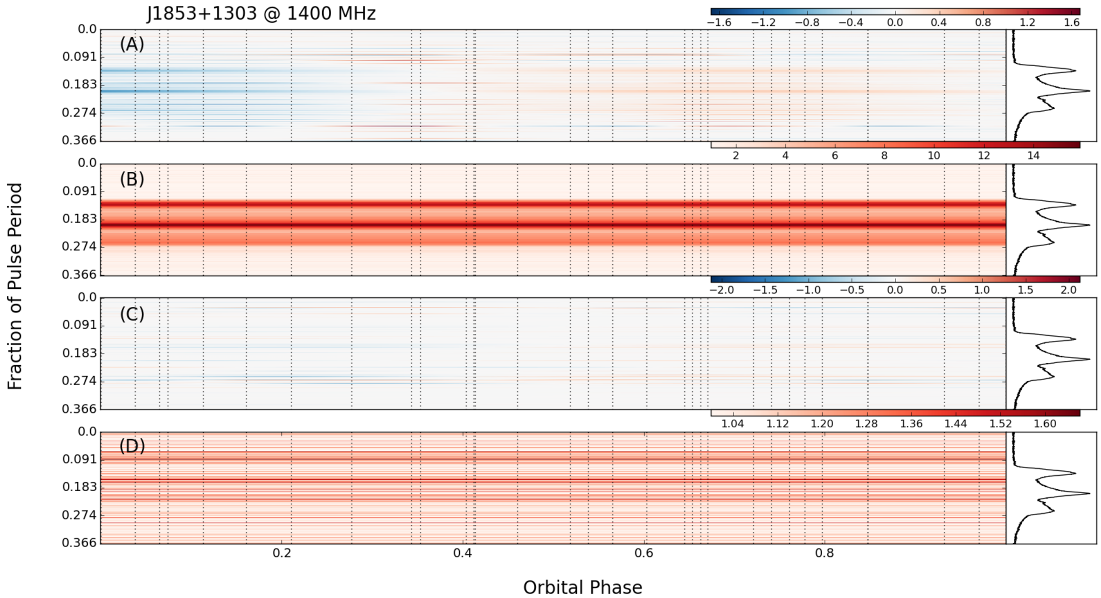

Figure 50: Variability maps for PSR J1853+1303 observed at 1400 MHz by AO. As described in Section 4.

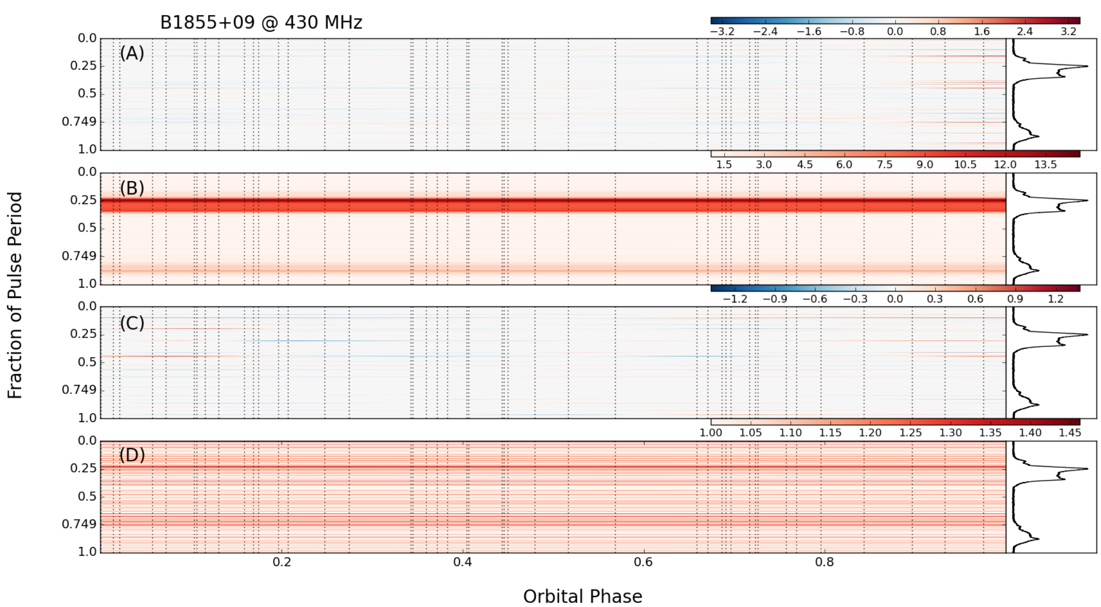

Figure 51: Variability maps for PSR B1855+09 observed at 430 MHz by AO. As described in Section 4.

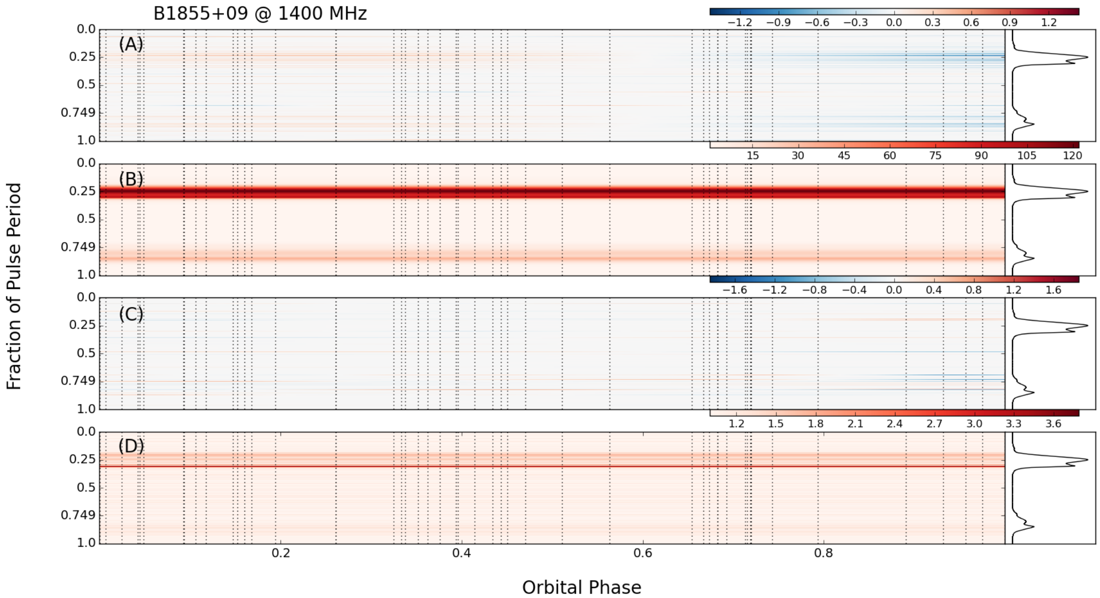

Figure 52: Variability maps for PSR B1855+09 observed at 1400 MHz by AO. As described in Section 4.

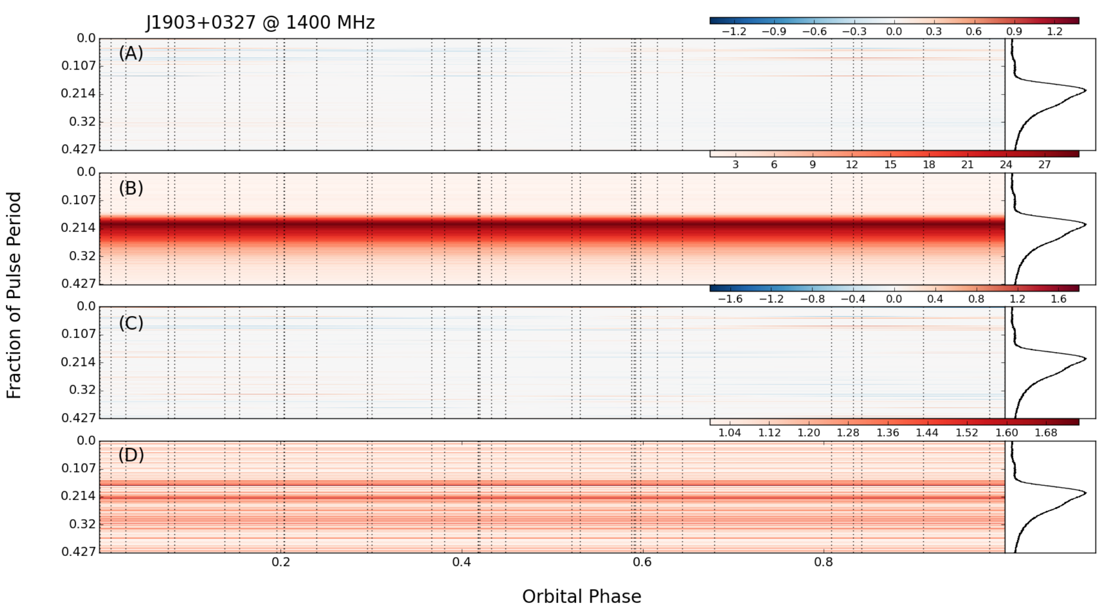

Figure 53: Variability maps for PSR J1903+0327 observed at 1400 MHz by AO. As described in Section 4.

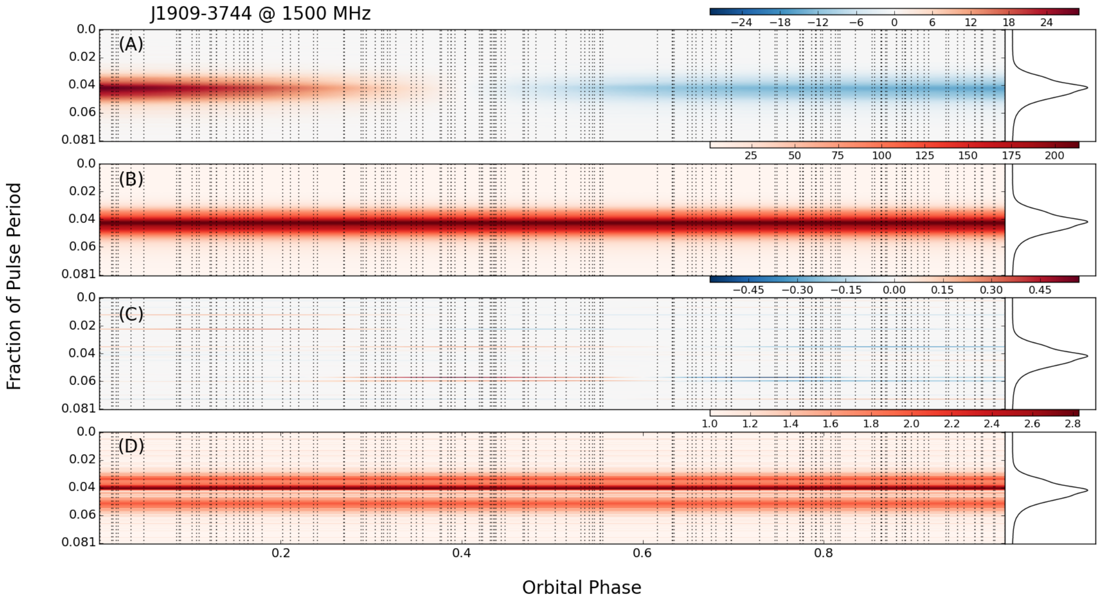

Figure 54: Variability maps for PSR J1909−3744 observed at 1500 MHz by the GBT. As described in Section 4.

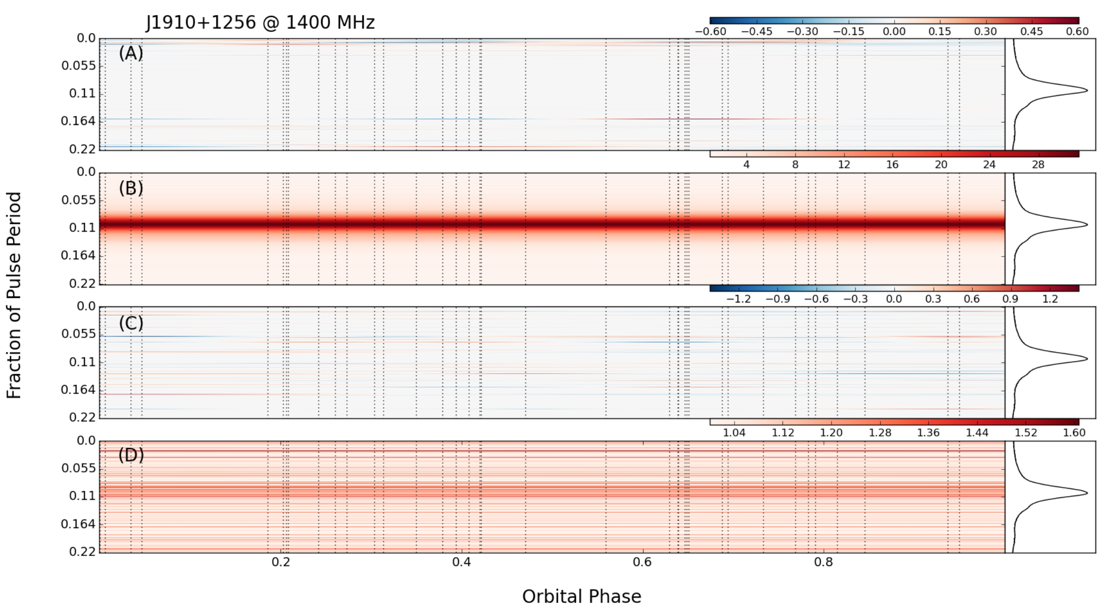

Figure 55: Variability maps for PSR J1910+1256 observed at 1400 MHz by AO. As described in Section 4.

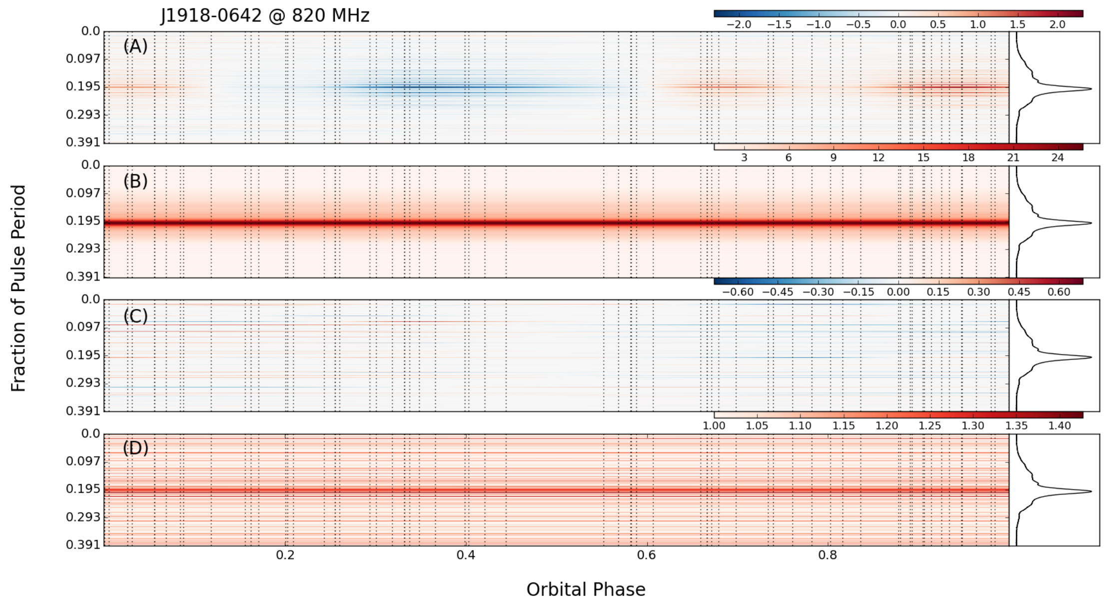

Figure 56: Variability maps for PSR J1918−0642 observed at 820 MHz by the GBT. As described in Section 4.

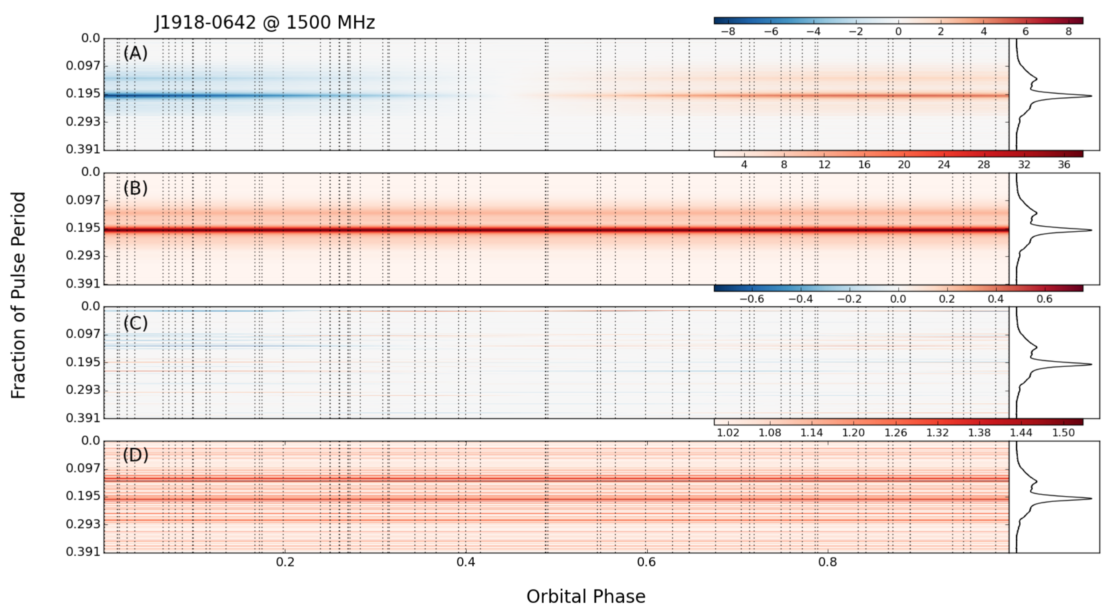

Figure 57: Variability maps for PSR J1918−0642 observed at 1500 MHz by the GBT. As described in Section 4.

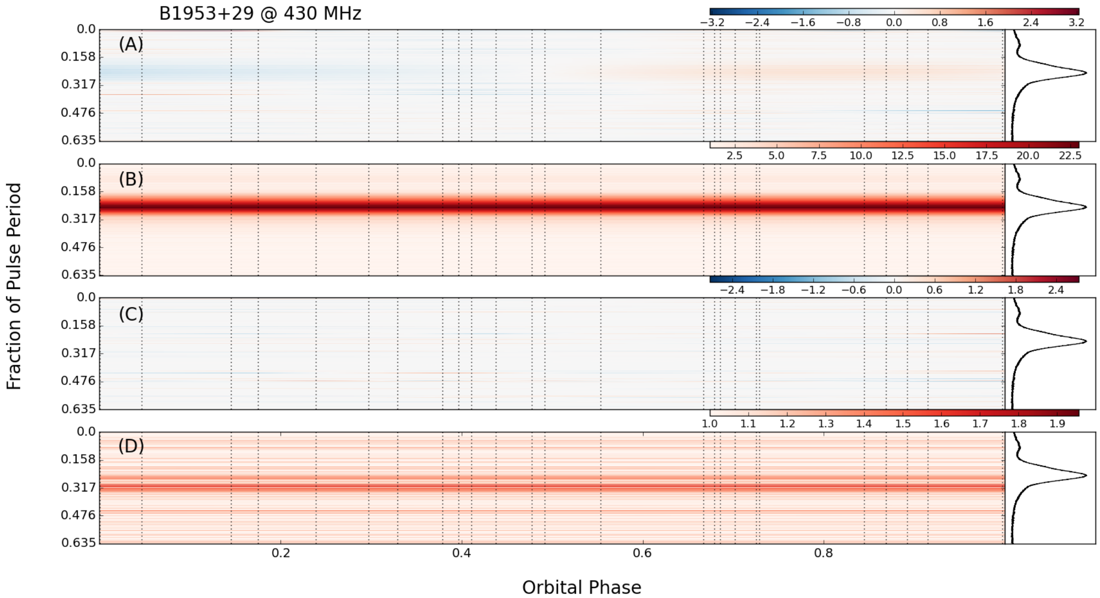

Figure 58: Variability maps for PSR B1953+29 observed at 430 MHz by AO. As described in Section 4.

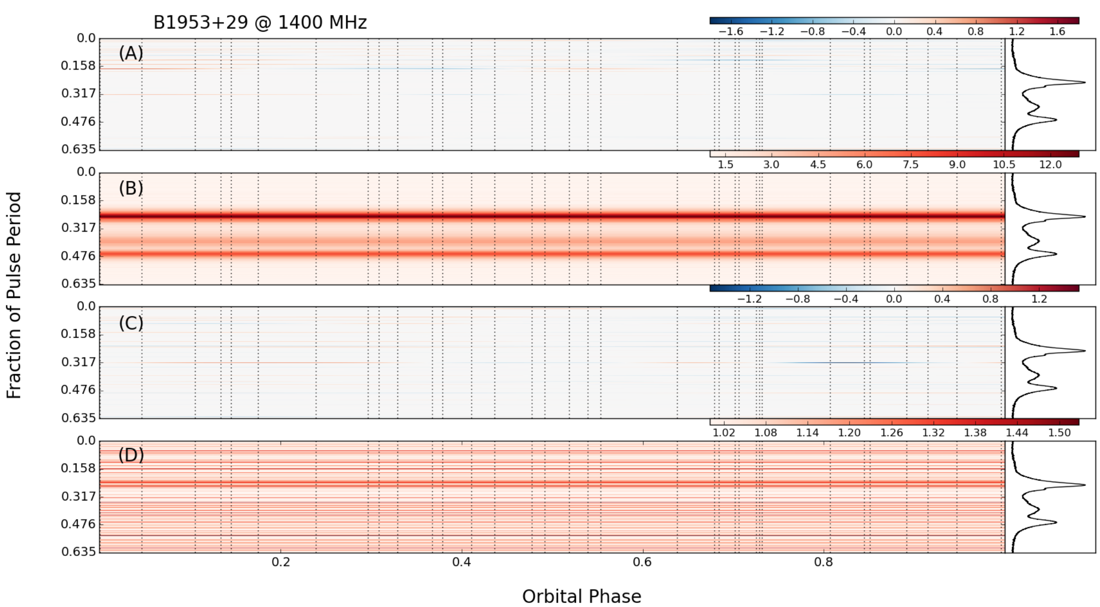

Figure 59: Variability maps for PSR B1953+29 observed at 1400 MHz by AO. As described in Section 4.

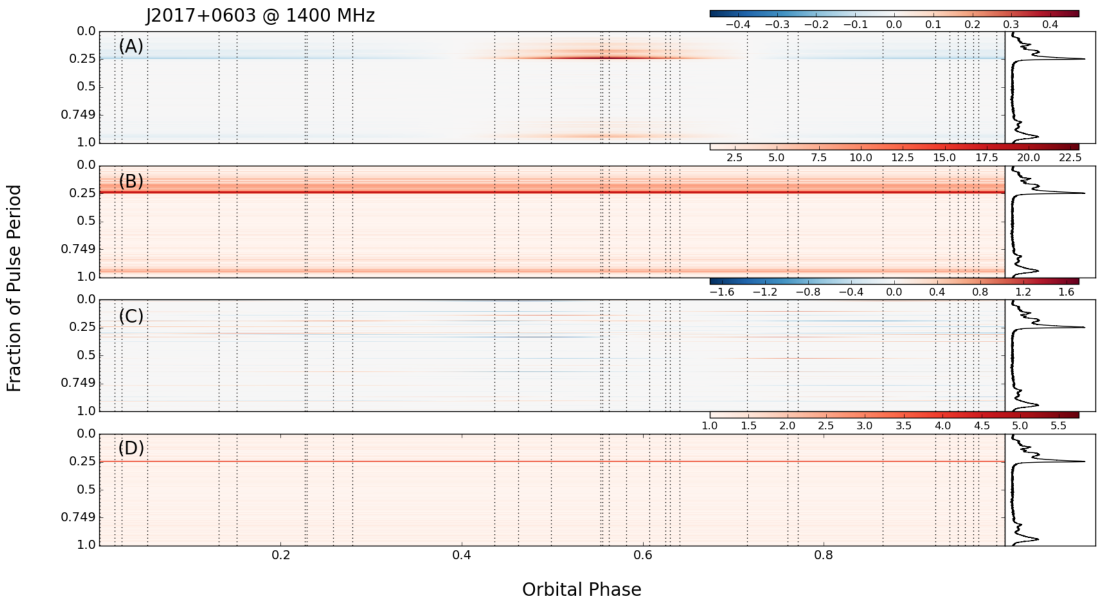

Figure 60: Variability maps for PSR J2017+0603 observed at 1400 MHz by AO. As described in Section 4.

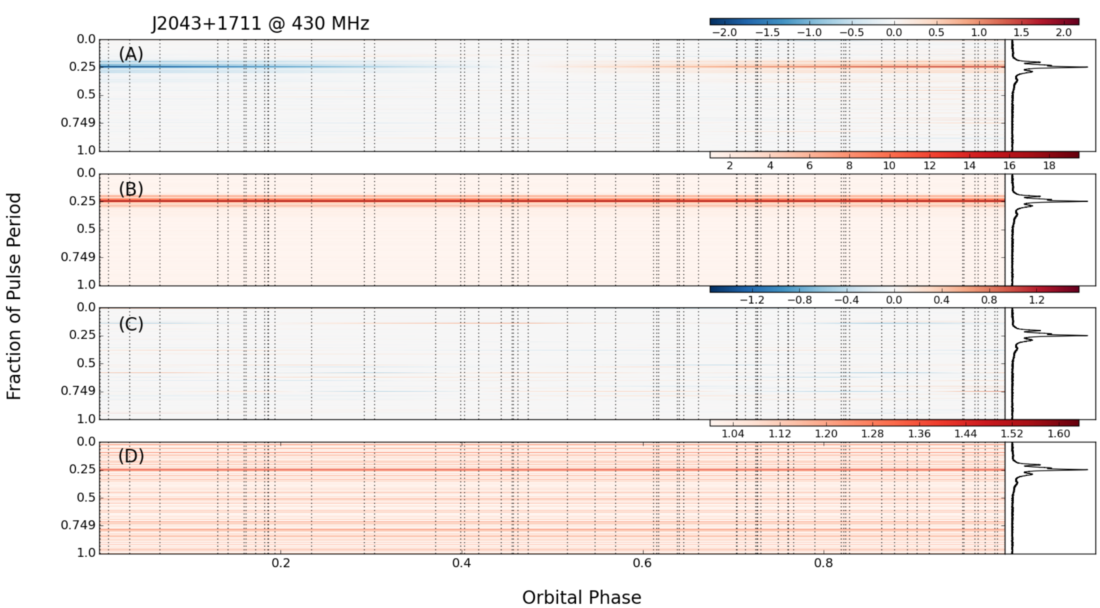

Figure 61: Variability maps for PSR J2043+1711 observed at 430 MHz by AO. As described in Section 4.

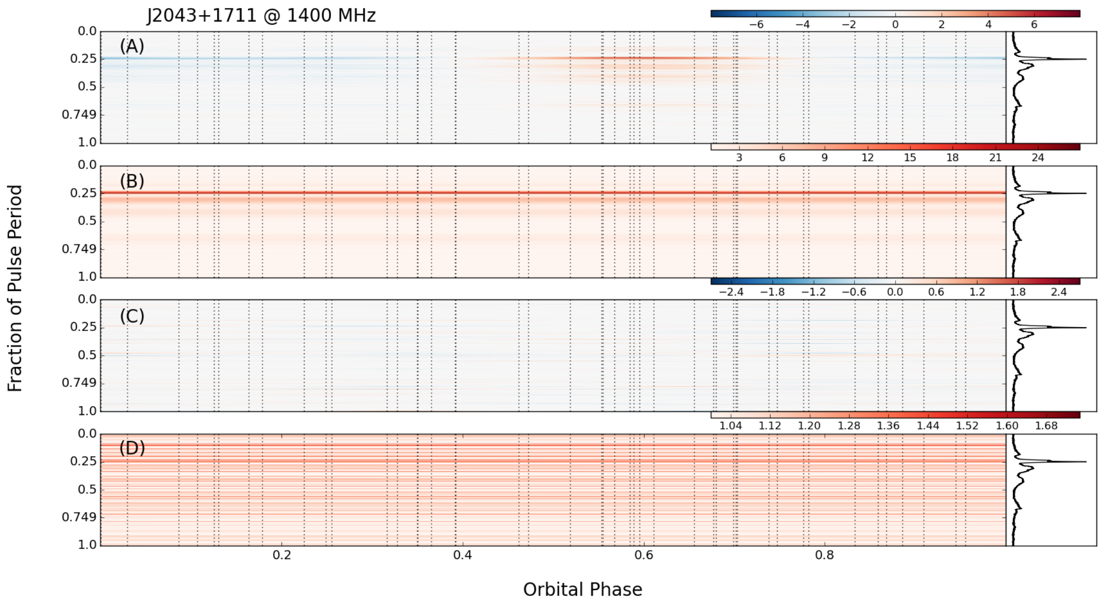

Figure 62: Variability maps for PSR J2043+1711 observed at 1400 MHz by AO. As described in Section 4.

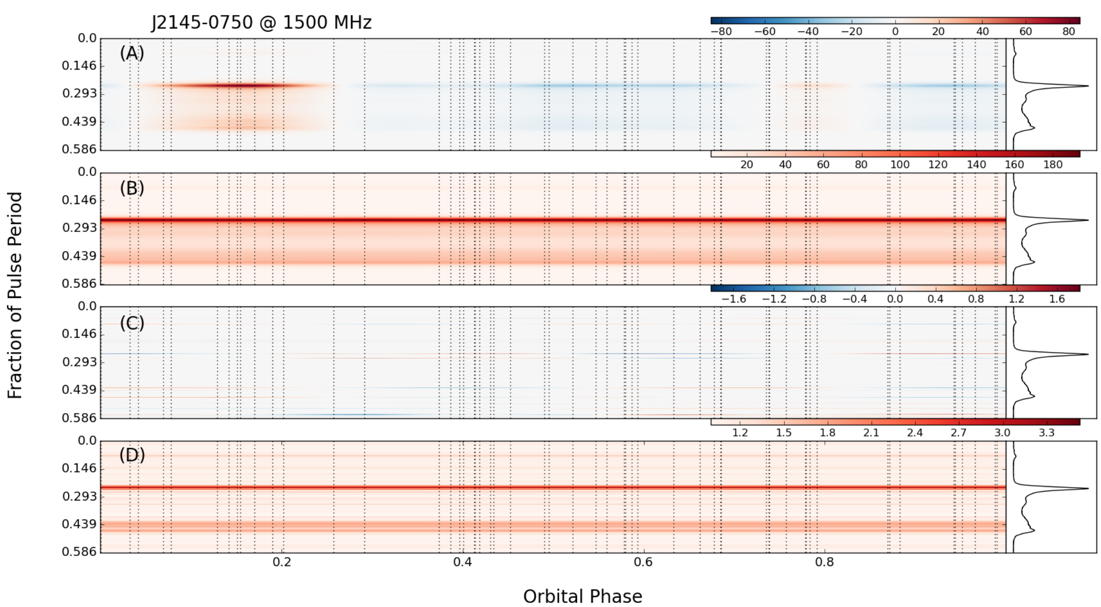

Figure 63: Variability maps for PSR J2145−0750 observed at 1500 MHz by the GBT. As described in Section 4.

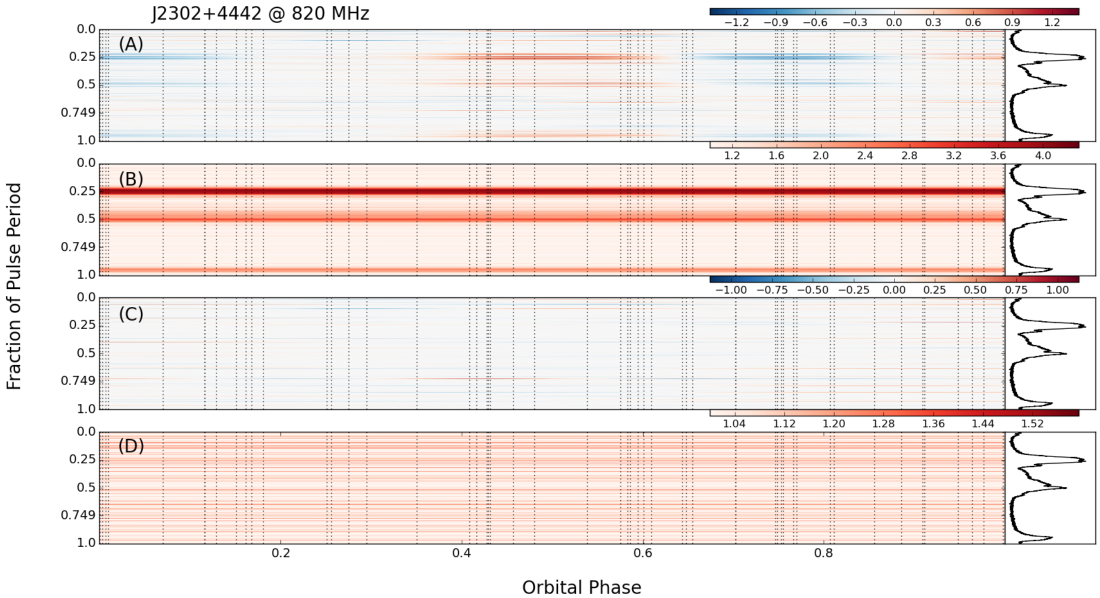

Figure 64: Variability maps for PSR J2302+4442 observed at 820 MHz by the GBT. As described in Section 4.

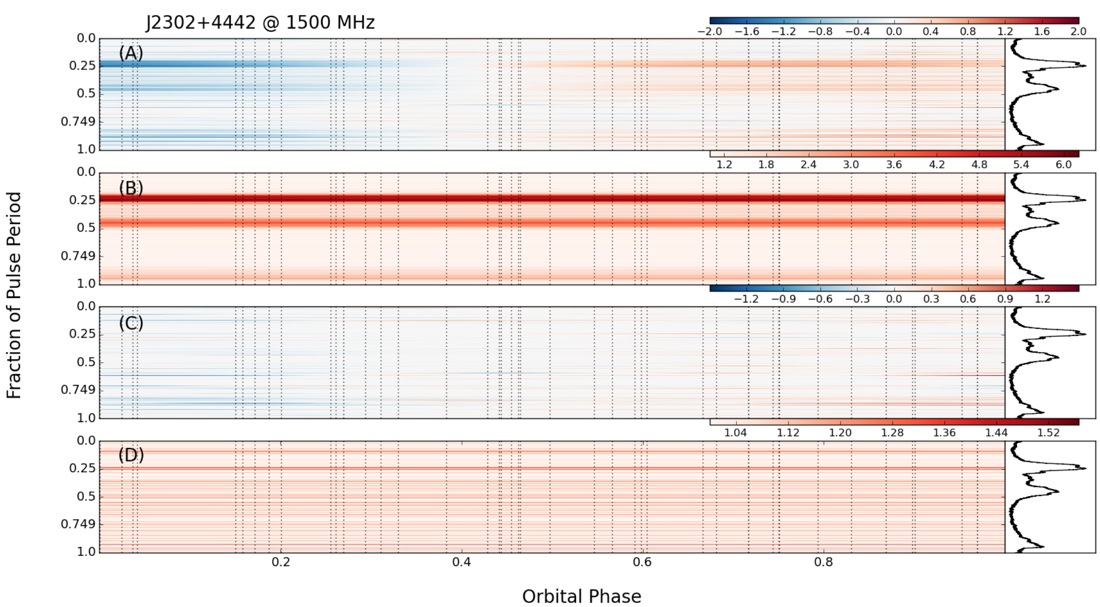

Figure 65: Variability maps for PSR J2302+4442 observed at 1500 MHz by the GBT. As described in Section 4.

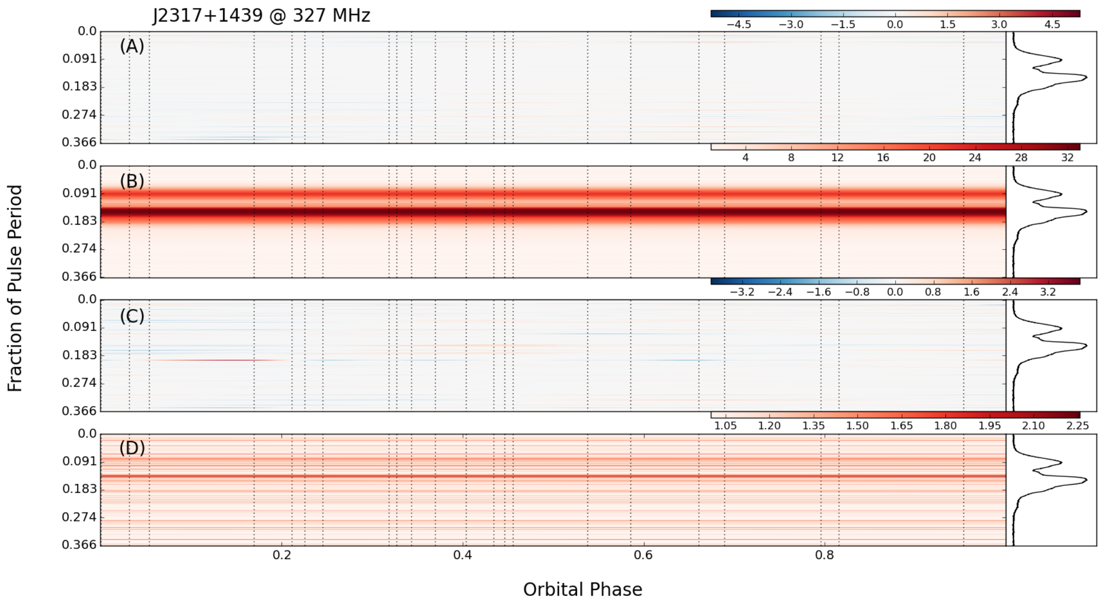

Figure 66: Variability maps for PSR J2317+1439 observed at 327 MHz by AO. As described in Section 4.

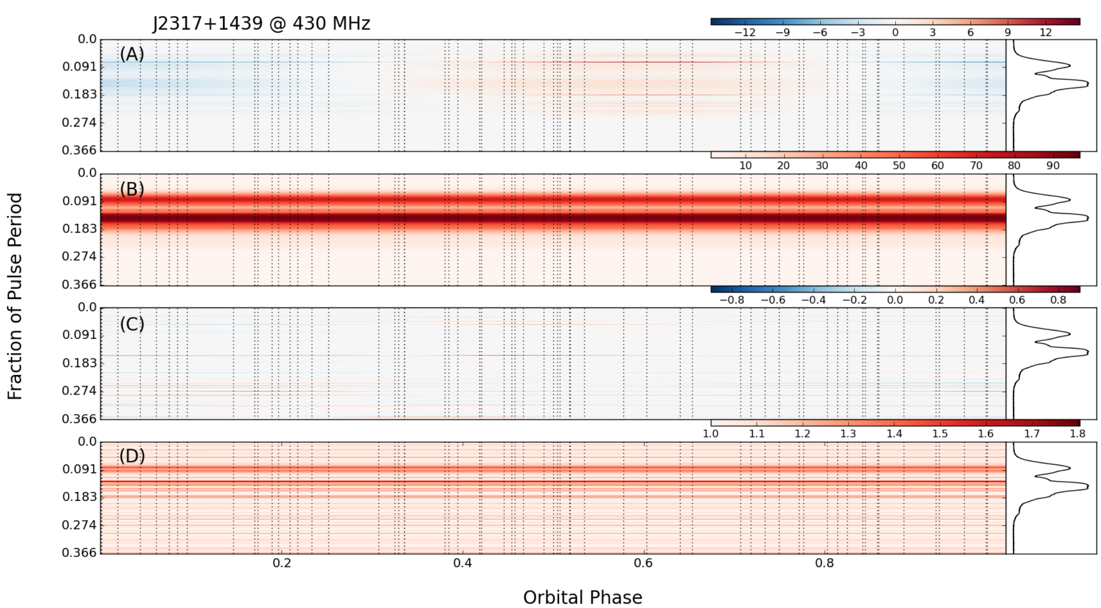

Figure 67: Variability maps for PSR J2317+1439 observed at 430 MHz by AO. As described in Section 4.

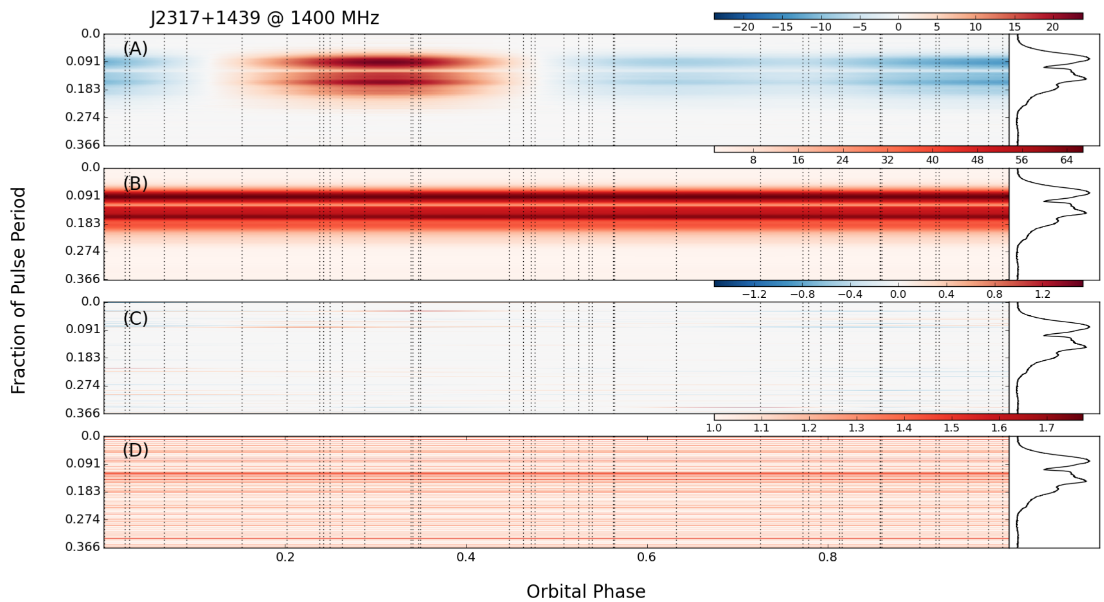

Figure 68: Variability maps for PSR J2317+1439 observed at 1400 MHz by AO. As described in Section 4.

6 Discussion & Conclusions

- We have analyzed the flux density and the pulse profile shape of 24 binary NANOGrav pulsars in 50 data sets and looked for significant changes as the pulsars orbit their companions. Only PSR J1713+0747 shows significant pulse profile shape changes and these are only seen in a few isolated profiles. For the AO observations carried out at 2030 MHz these profile shape changes seem to be caused by RFI (see Figure 14 and Section 5.1.5).

- 11 of the notable cases presented have flux density levels that show a systematic trend over their orbital period. These trends are either (i) low significance, (ii) primarily induced by isolated outlying data points, or both. Some outlying flux density data points are clearly due to miscalibration. All three data sets in which this miscalibration is seen are AO observations made at 2030 MHz (PSRs J1713+0747, J1738+0333 and J2214+3000).

- Three of the notible cases (PSR J1012+5307 at 1500 MHz, PSR J1909−3744 at 820 MHz, PSR J2145−0750 at 820 MHz) show trends over the pulsar orbit that seem to be influenced by multiple neighboring data points (rather than one or two outliers). However, the significance of these trends is low. As more data points are collected with each orbit, this will better inform the GP models; more data are needed to see if the slight trends persist. There are currently no strong trends that systematically occur over many consecutive data points. For PSR J1012+5307 a similar but lower significance trend to the 1500 MHz is seen at 820 MHz. For PSR J1909+3744 the 1500 MHz data set flux density trends doesn't match those at 820 MHz. For PSR J214−07505 the 1500 MHz data set flux density trends doesn't match those at 820 MHz.

- Of the 50 data sets analyzed, 29 were observed at AO and 21 by the GBT. However of the 12 notable cases in Section 5.1, 9 were observed at AO and only 3 by the GBT.

- As discussed in Section 3.2, the GP length scale has a lower bound of 0.1 of an orbit. If the data was re-analyzed with a smaller lower bound, the GP may model shorter timescale trends in some data sets. We set the lower limit with the assumption that the variability timescales should not be too short if they are to be attributal to the phase of a pulsar's orbit.

- We have shown that outlying data points can strongly influence the GP models. In future work, if non-astrophysical pulse profile changes can be confidently identified and removed, then re-analyzing the remaining data may reveal additional trends.

References

Arzoumanian, Z., Brazier, A., Burke-Spolaor, S., Chamberlin, S., Chatterjee, S., Christy, B., Cordes, J. M., Cornish, N., Crowter, K., Demorest, P. B., Dolch, T., Ellis, J. A., Ferdman, Fonseca, E., Garver-Daniels, N., Gonzalez, M. E., Jenet, F. A., Jones, G., Jones, M. L., Kaspi, V. M., Koop, M., Lam, M. T., Lazio, T. J. W., Levin, L., Lommen, A. N., Lorimer, D. R., Luo, J., Lynch, R. S., Madison, D., McLaughlin, M. A., McWilliams, S. T., Nice, D. J., Palliyaguru, N., Pennucci, T. T., Ransom, S. M., Siemens, X., Stairs, I. H., Stinebring, D. R., Stovall, K., Swiggum, J. K., Vallisneri, M., van Haasteren, R., Wang, Y., and Zhu, W. (2015). ApJ, 813:65.

Arzoumanian, Z., Brazier, A., Burke-Spolaor, S., Chamberlin, S., Chatterjee, S., Christy, B., Cordes, J. M., Cornish, N. J., Crawford, F., Thankful Cromartie, H., Crowter, K., DeCesar, M. E., Demorest, P. B., Dolch, T., Ellis, J. A., Ferdman, R. D., Ferrara, E. C., Fonseca, E., Garver-Daniels, N., Gentile, P. A., Halmrast, D., Huerta, E. A., Jenet, F. A., Jessup, C., Jones, G., Jones, M. L., Kaplan, D. L., Lam, M. T., Lazio, T. J. W., Levin, L., Lommen, A., Lorimer,

D. R., Luo, J., Lynch, R. S., Madison, D., Matthews, A. M., McLaughlin, M. A., McWilliams, S. T., Mingarelli, C., Ng, C., Nice, D. J., Pennucci, T. T., Ransom, S. M., Ray, P. S., Siemens, X., Simon, J., Spiewak, R., Stairs, I. H., Stinebring, D. R., Stovall, K., Swiggum, J. K., Taylor, S. R., Vallisneri, M., van Haasteren, R., Vigeland, S. J., Zhu, W., and The NANOGrav Collaboration (2018). ApJS, 235:37.

Brook, P. R., Karastergiou, A., McLaughlin, M. A., Lam, M. T., Arzoumanian, Z., Chatterjee, S., Cordes, J. M., Crowter, K., DeCesar, M., Demorest, P. B., Dolch, T., Ellis, J. A., Ferdman, R. D., Ferrara, E., Fonseca, E., Gentile, P. A., Jones, G., Jones, M. L., Lazio, T. J. W., Levin, L., Lorimer, D. R., Lynch, R. S., Ng, C., Nice, D. J., Pennucci, T. T., Ransom, S. M., Ray, P. S., Spiewak, R., Stairs, I. H., Stinebring, D. R., Stovall, K., Swiggum, J. K., and Zhu, W. W. (2018). The NANOGrav 11-year Data Set: Pulse Profile Variability. ApJ, 868:122.

Camilo, F., Ransom, S. M., Chatterjee, S., Johnston, S., and Demorest, P. (2012). ApJ, 746:63.

DuPlain, R., Ransom, S., Demorest, P., Brandt, P., Ford, J., and Shelton, A. L. (2008). Launching GUPPI: the Green Bank Ultimate Pulsar Processing Instrument. In *Advanced Software and Control for Astronomy II*, volume 7019 of Proc. SPIE, page 70191D.

Fonseca, E., Pennucci, T. T., Ellis, J. A., Stairs, I. H., Nice, D. J., Ransom, S. M., Demorest, P. B., Arzoumanian, Z., Crowter, K., Dolch, T., Ferdman, R. D., Gonzalez, M. E., Jones, G., Jones, M. L., Lam, M. T., Levin, L., McLaughlin, M. A., Stovall, K., Swiggum, J. K., and Zhu, W. (2016). The NANOGrav Nine-year Data Set: Mass and Geometric Measurements of Binary Millisecond Pulsars. ApJ, 832:167.

Ford, J. M., Demorest, P., and Ransom, S. (2010). Heterogeneous real-time computing in radio astronomy. In *Software and Cyberinfrastructure for Astronomy*, volume 7740 of Proc. SPIE, page 77400A.

Gentile, P. A., McLaughlin, M. A., Demorest, P. B., Stairs, I. H., Arzoumanian, Z., Crowter, K., Dolch, T., DeCesar, M. E., Ellis, J. A., Ferdman, R. D., Ferrara, E. C., Fonseca, E., Gonzalez, M. E., Jones, G., Jones, M. L., Lam, M. T., Levin, L., Lorimer, D. R., Lynch, R. S., Ng, C., Nice, D. J., Pennucci, T. T., Ransom, S. M., Ray, P. S., Spiewak, R., Stovall, K., Swiggum,

J. K., and Zhu, W. (2018). The NANOGrav 11 yr Data Set: Arecibo Observatory Polarimetry and Pulse Microcomponents. ApJ, 862:47.

Hotan, A. W., Bailes, M., and Ord, S. M. (2005). Geodetic Precession in PSR J1141-6545. ApJ, 624:906–913.

Kramer, M. (1998). Determination of the Geometry of the PSR B1913+16 System by Geodetic Precession. ApJ, 509:856–860.

Kramer, M., Lyne, A. G., O'Brien, J. T., Jordan, C. A., and Lorimer, D. R. (2006). A Periodically Active Pulsar Giving Insight into Magnetospheric Physics. *Science*, 312:549–551.

Lorimer, D. R., Lyne, A. G., McLaughlin, M. A., Kramer, M., Pavlov, G. G., and Chang, C. (2012). ApJ, 758:141.

Lyne, A., Hobbs, G., Kramer, M., Stairs, I., and Stappers, B. (2010). *Science*, 329:408.

Lyne, A. G., Stappers, B. W., Freire, P. C. C., Hessels, J. W. T., Kaspi, V. M., Allen, B., Bogdanov, S., Brazier, A., Camilo, F., Cardoso, F., Chatterjee, S., Cordes, J. M., Crawford, F., Deneva, J. S., Ferdman, R. D., Jenet, F. A., Knispel, B., Lazarus, P., van Leeuwen, J., Lynch, R., Madsen, E., McLaughlin, M. A., Parent, E., Patel, C., Ransom, S. M., Scholz, P., Seymour, A., Siemens, X., Spitler, L. G., Stairs, I. H., Stovall, K., Swiggum, J., Wharton, R. S., and Zhu, W. W. (2017). ApJ, 834:72.

Pennucci, T. T., Demorest, P. B., and Ransom, S. M. (2014). Elementary Wideband Timing of Radio Pulsars. ApJ, 790:93.

Stairs, I. H., Lyne, A. G., and Shemar, S. L. (2000). Evidence for free precession in a pulsar. Nature, 406:484–486.